Upper Limits of Active Galactic Nuclei observed by the MAGIC telescopes

Nikolić, Lisa

UNIVERSITY OF RIJEKA
FACULTY OF PHYSICS

Lisa Nikolić

Upper Limits of Active Galactic Nuclei observed by the MAGIC telescopes

Master's thesis

Rijeka, 2022.

UNIVERSITY OF RIJEKA
FACULTY OF PHYSICS

Master of Physics, curriculum Astrophysics and elementary particle physics

Lisa Nikolić

Upper Limits of Active Galactic Nuclei observed by the MAGIC telescopes

Master's thesis

Supervisor:
prof. dr. sc. Dijana Dominis Prester

Rijeka, 2022.

SVEUČILIŠTE U RIJECI
FAKULTET ZA FIZIKU

Diplomski studij Fizika, smjer Astrofizika i fizika elementarnih čestica

Lisa Nikolić

Gornje granice detekcije Aktivnih Galaktičkih Jezgri opažanih teleskopima MAGIC

Diplomski rad

Mentor:
prof. dr. sc. Dijana Dominis Prester

Rijeka, 2022.

Contents

ABSTRACT

Blazars are Active Galactic Nuclei (AGNs) whose jet is pointed towards the observer. They are usually divided in two sub-classes, depending on the aspect of their optical spectrum. Blazars which present an optical spectrum which lacks of emission lines are categorised as BL Lacertae objects (BL Lacs), while blazars whose optical spectrum shows strong emission lines are named Flat Spectrum Radio Quasars (FSRQs). The majority of blazars who have been found emitting VHE γ-rays are BL Lacs. MAGIC observed and discovered in the VHE γ-ray band many of them in the past years. Nevertheless some of them remained undetected, meaning the significance of the signal was lower than 5 σ.

For my work of thesis, I gathered information and data from such undetected sources and created a catalog of 41 sources, 25 of which are BL Lacs. From them, I selected a sample of 5 sources which were observed in 2020-2022 as a starting point for a more complete upper limits study which is in preparation within the MAGIC collaboration. The sources I analysed in detail are: 4FGL-J0955.1+3551, 87GB-225250.5+235403, TXS1700+685, PKS2247-131 and PKS2345-16.

From the selected sample of sources I obtained upper limits (ULs) to the light curves (LCs) and spectral energy distributions (SEDs), which can be used in the future to study such sources in a multi-wavelength (MWL) context and define a baseline for future studies in case of detection. ULs can in fact, combined with other MWL data, help in understanding the possible emission scenarios of those sources and into defining strategies to detect them.

Key words: very-high-energy gamma rays, AGN , very-high-energy-astrophysics, MAGIC telescopes, astrophysics, astronomy, blazars, black holes

SAŽETAK

Blazari su Aktivne Galaktičke Jezgre (AGN) čiji je mlaz uperen prema promatraču. Uobičajeno su podijeljeni u dvije klase ovisno o svojstvima njihova optičkog spektra. Blazari koji imaju optički spektar u kojem nedostaju emisijske linije kategorizirani su kao BL Lacertae objekt (BL Lac), dok se blazari, čiji optički spektar ima jake emisijske linije, nazivaju Flat Spectrum Radio Quasars (FSRQ). Većina blazara koji emitiraju VHE (eng. very high energy) γ-zrake su BL Lac objekti. U proteklim godinama mnogo ih je promatrano i otkriveno sa MAGIC teleskopima. Ipak, neki izvori i dalje ostaju nedetektirani, na što upućuje podatak da je značajnost manja od 5σ.

U svojem radu prikupila sam informacije i podatke upravo od takvih nedetektiranih izvora i stvorila katalog koji sadrzi 41 izvor, od kojih su 25 BL Lac objekti. Potom sam izdvojila uzorak od 5 izvora koji su bili promatrani u periodu od 2020. do 2022. godine i to mi je bila početna točka za detaljniju analizu gornjih granica detekcije koja je u pripremi s kolaboracijom MAGIC. Izvori koje sam detaljnije analizirala su: 4FGL-J0955.1+3551, 87GB-225250.5+235403, TXS1700+685, PKS2247-131 i PKS2345-16.

Iz odabranog uzorka uspjela sam odrediti gornje granice detekcije za svjetlosne krivulje i spektralnu distribuciju energije. Ti podatci se u budućnosti mogu upotrijebiti za promatranje sličnih izvora u kontekstu istraživanja u cijelom području elektromagnetskog spektra, i mogu poslužiti kao vodilja u slučaju detekcije. Gornje granice, u kombinaciji sa podatcima u ostalim područjima spektra, mogu pomoći pri razumijevanju moguće emisije za te izvore baš te za određivanje mogućih strategija za detekciju.

Ključne riječi: gama zračenje vrlo visokih energija, aktivne galaktičke jezgre, astrofizika vrlo visokih energija, teleskopi MAGIC, astrofizika, astronomija, blazari, crne rupe

ACKNOWLEDGEMENTS

Foremost I would like to thank my mentor, prof. dr. sc. Dijana Dominis Prester, for entrusting me with this work of thesis and encouraging me to grow and make new connections. Thank you for the opportunity to experience how is it like to be a part of a collaboration.

I would like to express immense gratitude to doc. dr. sc. Marina Manganaro for offering me her time and patience, and for pushing me forwards when challenges occurred. I really appreciate all the guidance that you have given me.

Also I would like to thank Lena Linhoff and Simone Mender for their assistance and advice during the analysis.

And least, but definitely not last, I want to express heartfelt thanks my family, friends, loved one and colleagues for always supporting me and being by my side in all times.

1 INTRODUCTION

Astroparticle physics is the field connecting astrophysics and particle physics. Many celestial objects are powerful accelerators of particles and their observation is the focus of high energy astronomy. With the availability of new technology and the birth of new instrumentation, other messengers became part of the picture: not only photons, but also neutrinos [1], cosmic rays and gravitational waves [2] can be detected from astrophysical objects. The emission of photons through the entire electromagnetic (EM) spectrum can be registered by instruments that work at different bands. Photons at energies above 100keV are called γ-rays. They are divided into six energy bands:

- Low energy (LE): $100keV < E < 100MeV$
- High energy (HE): $100MeV < E < 100GeV$
- Very high energy (VHE): $100GeV < E < 100TeV$
- Ultra high energy (UHE): $100TeV < E < 100PeV$
- Extremely high energy (EHE): $E > 100PeV$

Observations of a same target performed by different telescopes are object of multi-wavelength (MWL) studies, nowadays the best tool to understand the emission mechanism of astrophysical sources. Since the Earth's atmosphere is opaque at some wavelengths (see Fig. 1) observations from space are necessary to obtain the full picture of a source.

This work of thesis is organised as follows:
The categorization and description of AGNs properties is presented in Sec. 2.
Sec. 3 is devoted to the description of the MAGIC telescopes, whose data were used in this thesis. The section describes the detection technique of MAGIC and in general of Imaging Atmospheric Cherenkov detectors (IACTs).
Sec. 4 is dedicated to the data analysis, and contains the information on the analysis chain performed for this work of the thesis on the selected sample of sources.
In Sec. 5, the results of the analysis are presented, and finally conclusions are drawn in Sec. 6.

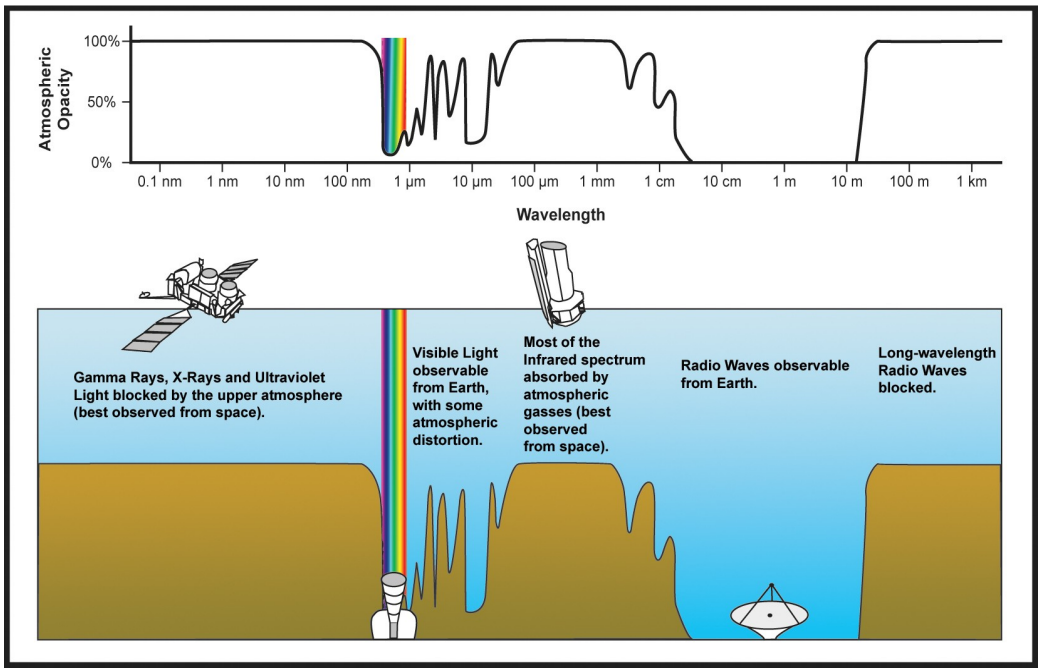

Figure 1: Opacity of Earth's atmosphere for different EM radiation wavelengths. (Credit: NASA)

2 ACTIVE GALACTIC NUCLEI (AGN)

The unified model states that the orientation of the torus and jets in relation to our line of sight determines the sort of active galaxy we observe.

The observational classification of AGN, dominated by the dichotomy between radio-quiet and radio-loud classes, with the latter constituting 10% of the population, is represented in Fig. 3.

2.1 Paradigm

2.1.1 Black Hole (BH)

In most galaxy centers there is located a supermassive black hole (SMBH) that has a mass $\sim 10^6 - 10^{10} M_\odot$ [3]. In roughly 1% of those galaxies the black hole can be active. That is seen by strong emission and accretion thus the name AGN. The amount of matter streaming on the black hole changes over time, and this variation determines the intensity of nucleus activity. We learn about this spatially unsolved area through the emission of matter from the black hole's immediate vicinity as

there is a loss of energy and angular momentum with matter input [4]. The area around the active nucleus is really extremely chaotic, with outflow complementing intake and the atmosphere being partially encircled by clouds that are constantly shifting.

2.1.2 Accretion disk

When material enters the center black hole, it will maintain its angular momentum and create an accretion disk that rotates around the BH [3]. The magnetic field intensity, the accretion rate, the existence or absence of a disk corona, and jets are only a few of the variables that affect the accretion disk's complex structure [5].

It is possible to determine the spectra of the accretion disk for variety of BH masses, spins and Eddington ratios [4]. It has been predicted that the matter that is falling toward the BH is transforming an significant portion of gravitational potential energy in kinetic energy. Thermal radiation is produced by in-falling matter that has been intensely heated inside an accretion disk near to the black hole's center. Inverse Compton effect on the photons of the heated corona can be produced by accelerated electrons. These processes primarily create radiation in the X-ray, optical and UV bands.

This type of AGN are also known as Seyfert galaxies. They are radio-weak and exhibit continuous emission in the optical range from the core area. Additionally, they occasionally emit powerful X-rays, narrow and sometimes broad emission lines, and a faint radio jet. Seyferts' host galaxies are often spiral galaxies [6].

2.1.3 Broad Line Region (BLR)

The most distinguishing characteristics of AGN are broad emission lines in the UV and optical bands. Doppler shifts cause these emission lines to widen, thus the name "broad line area" for this region.

They are not present in all AGN; sources that have them are categorized as type 1 AGN, whereas those without broad lines are categorized as type 2 AGN. Although the Type 2 AGN, that appear to belong to low luminosity AGN, really do lack BLR there are some Type 2 AGN where the BLR can be obscured in the background of dusty/molecular toruses. It is not always simple to rule out the presence of the concealed BLR [4].

The BH is surrounded with BLR clouds that have speed of a few thousand kilometers per second. The clouds typically have a radius of $10^{14}m$ and temperature of 10^4 K due to the powerful radiation [3].

By combining the velocity and the effective radius of the BLR obtained from time delay measurements, we can derive the black hole mass using Kepler's law.

BLR is usually being positioned further away from the BH and accretion disk, but that isn't necessarily correct. For wind based models, BLR region will always be a disk, but if there is a cloud inflow from greater distances then that isn't the case. It is difficult to determine from observations whether clouds are present on both sides of the equatorial plane (no disk) or solely above (those below can not be seen because of the disk) [4].

2.1.4 Narrow Line Region (NLR)

Narrow line region is interesting for several reasons, one of them being that their dynamics might lead to an explanation how the AGN is functioning. It is also the only AGN component that can be spatially resolved in the optical, which is significant because the NLR receives non-isotropic illumination from the central source. Furthermore, ionizing radiation coming from the source prevails over any other sources making it the largest spacial scale to do so [5].

NLR is a region of somewhat less thick gas clouds than the BLR, and located farther from the BH ($\sim$ 100pc). The NLR is sufficiently removed from the center for the bulge to control its dynamics [7]. In addition, the clouds have lower velocities ($\sim$ 300 kilometers per second) than those in BLR.

2.1.5 Torus

The SMBH and the accretion disk are enclosed by toroidal shaped matter, approximately one to ten parsecs away. The radiation that comes from SMBH, accretion disk and BLR is obscured by the torus and then re-emitted in the IR band. Also the torus is located where SMBH gravity predominates over that of the galactic bulge [8].

2.1.6 Jet

The matter that falls into the SMBH in about 10% of AGNs leads to formation of powerful jets that are ejected in oppposite directions. It is not rare for them to come out only on one side, or for the second jet to be much fainter when they are present on both sides [5]. The jet (or jets) are moving at relativistic speed and are usually perpendicular to the accretion disk [3]. They can reach distances up to a few kpc (or occasionally up to Mpc) and are believed to have their origins close to the SMBH.

Jets are accelerators that produce highly energetic particles with relativistic speed that are then observed as non-thermal emission. This radiation can be seen in the entire EM spectrum (radio to γ-rays). The radio-loud AGN's luminosity is dominated by the emission produced by the jet(s). This emission can be dismissed for radio-quiet AGNs [6].

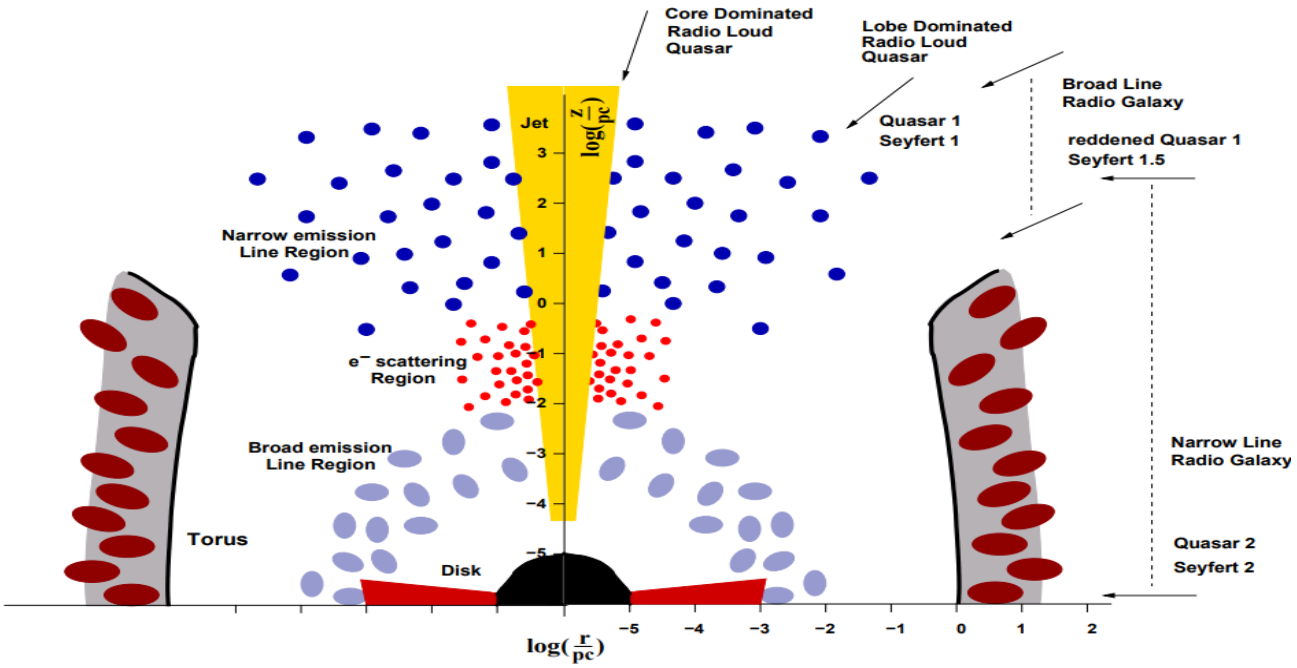

Figure 2: Illustration of the symmetrically cylindrical AGN with main parts labeled. (Image taken from: [9])

2.2 Radio-quiet AGN

2.2.1 Seyfert

The emission from Seyfert galaxies is anticipated if the jet is not pointed in the direction of the observer [3]. Continuum emission as well as strong broad emission lines are expected to be seen [10]. They also have lower luminosity than other AGN types.

Two different subclasses were distinguished after realizing there are differences in Balmer lines and forbidden lines' respective widths [11]. In Seyfert 1 galaxies there are several emission lines, whereas in Seyfert 2 galaxies only narrow lines can be seen. With spectrum quality improvements it became clear that other Seyfert subclasses also exist. Depending on the relative intensities of the broad and narrow-line features the galaxies have been classified as Seyfert 1, 1.5, 1.8, 1.9, 2 [10].

2.2.2 QSO

Radio surveys in the 1950s led to the initial discovery of quasars. Due to the lack of knowledge on the actual makeup of these bright stars-like objects, they were first referred to as "quasi-stellar radio sources" or "quasi-stellar objects" (QSO), which was then abbreviated to "quasars." They are some of

most luminous objects observed at every wavelength [5].

As opposed to Seyfert galaxies, quasars have smaller angular sizes ($\sim$ 7"). They have larger redshifts, and a large UV flux (this information is used a detection technique [10]) as well as broad SED [5]. Also, the number of QSOs is found to be 10–20 times higher than their radio-loud counterparts [5].

2.3 Radio-loud AGN

Jet dominated AGN are usually correlated to radio-loud AGN [6]. There are several classes in regard to jet orientation toward the observer.

2.3.1 Radio galaxies

Radio galaxies and blazars are equivalents. What differentiates them is the angle at which the jet is observed. Additionally radio galaxies have higher density ($\sim 10^3$) than blazars [12]. There are fewer radio-loud than radio-quiet sources, however they are several magnitudes brighter in the radio part of the spectrum [12].

Radio galaxies can further be separated into two different luminosity classes, named after Fanaroff and Riley that made that distinction [13]. The weaker class are FR I sources characterized with a bright center that diminishes when moving closer to the edges [5]. They are thought to be BL Lacertae objects (BL Lacs') misaligned counterparts. FR II are more luminous class that frequently exhibits regions of heightened emission from within the source or from their edges. Therefore this class is persumed to be a Flat Spectrum Radio Quasar (FSRQ) counterpart [12].

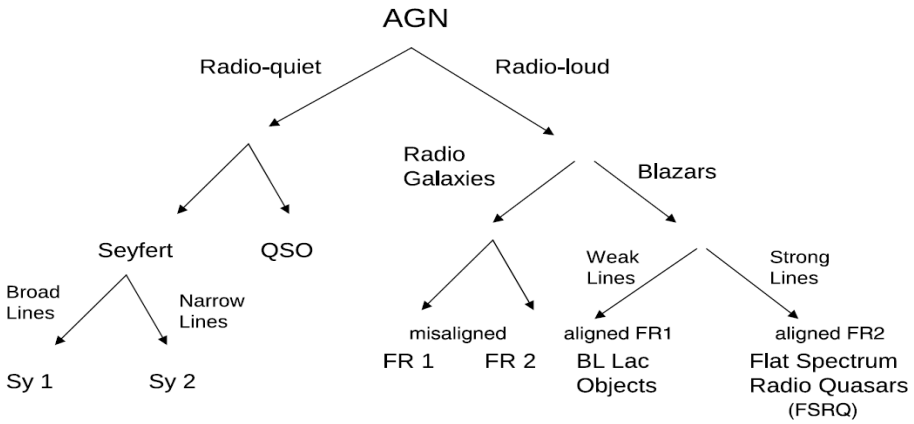

Figure 3: Classification of active galaxies based on observation described in chapters 2.2 and 2.3. (Image taken from [12])

2.3.2 Blazars

Blazars are rapidly variable sources, whose jet is pointed directly towards the observer [6]. They are intriguing sources since the particles in the jet are accelerated to the highest energies.

A common categorization of blazars is based on synchrotron SED frequency peak resulting in LSP (low-synchrotron-peaked), ISP (intermediate-synchrotron-peaked) and HSP (high-synchrotron-peaked) blazars with frequencies of $\nu_L < 1014$ Hz, 1014 Hz $< \nu_I <$ 1015 Hz, 1015 Hz $< \nu_H$ respectively [12]. Another distinction is made according to their spectral characteristics in the optical band:

2.3.2.1 FSRQ are blazars that in their optical spectrum show broad emission lines. That is an indicator of existing compact material in BLR and radiation from accretion disk. By having a fast falling spectra it is not likely for FSRQs to have significant fluxes above TeV energies. Being classified as LSP blazar contributes to that assumption. Furthermore it can be said that FSRQs are objects of highest luminosities [12].

2.3.2.2 BL Lac objects , unlike FSRQs do not have or have insignificant broad lines, dusty torus or accretion disk [12]. Their synchrotron peak is occupying higher energies than the one in FSRQs leading to another classification: LBL (low-energy peaked BL Lacs), IBL (intermediate-energy peaked BL Lacs) and HBL (high-energy peaked BL Lacs) [3]. Since γ-ray energy peak is located at several GeV's BL Lacs are VHE γ-ray sources as well as HSP blazars.

Blazars are uncommon in the local universe, with the spatial density of BL Lacss being little more than $\sim (10^2 - 10^3) Gpc^{-3}$ [12]. Furthermore, BL Lacs have lower-luminosity.

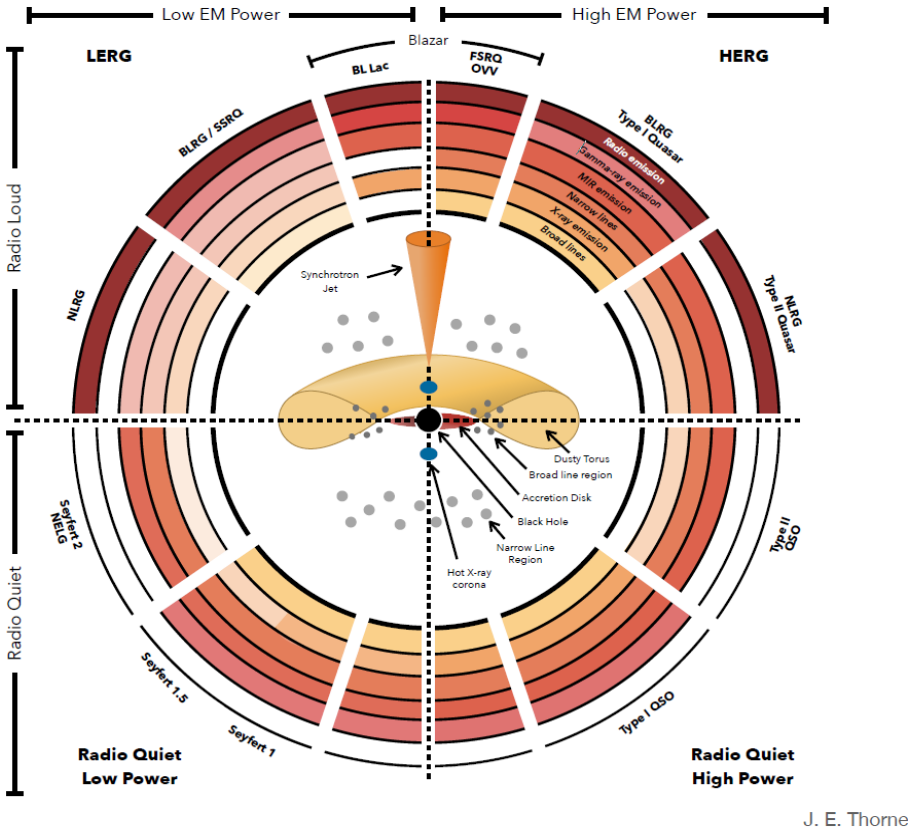

Figure 4: AGN unification diagram. (Credit: Jessica Thorne (https://zenodo.org/record/6381013))

3 MAGIC TELESCOPES

MAGIC is a system of two Imaging Atmospheric Gamma-ray Cherenkov telescopes (IACTs), located at the Roque de Los Muchachos Observatory, in the Canary island of La Palma. In this work of thesis I analyzed MAGIC data from several AGNs and in this section an overview of the detection technique and characteristics of this instrument is given.

3.1 Air showers

Extensive Air Showers (EAS) develop in the atmosphere when an energetic particle interacts with atomic nuclei. A EAS generated by a γ ray has a very regular shape with respect to a EAS generated

by a charged particle, like a proton or a muon. The development of showers in the atmosphere is very important for the study of gamma-rays from astrophysical sources and of course for the study of cosmic rays. Due to the different shapes it is possible to discriminate between showers originated by gamma-rays or by hadrons with a very good precision. In this discrimination the main parameters which define the showers characteristic were introduced by Hillas and they are named after him [14]. In Fig. 5 air showers generated by a γ ray of energy 100GeV (left) and by a 100GeV proton are shown. Together with the longitudinal development, also a top view is presented (at the bottom right of each longitudinal view). The simulations were obtained with the program Corsika (COsmic Ray SImulations for KAscade) [1].

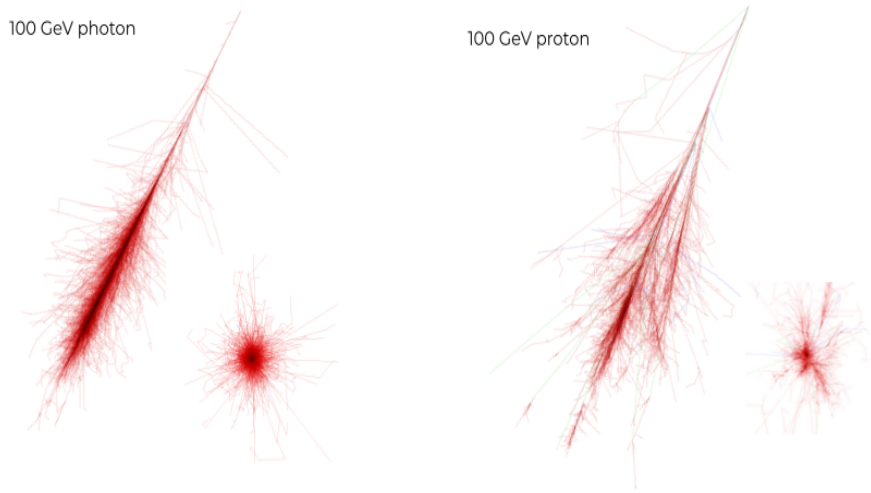

Figure 5: Simulation of Air showers initiated respectively by a gamma of 100GeV and a proton of 100GeV. Obtained with the program Corsika (https://www.iap.kit.edu/corsika/). (Credit: Fabian Schmidt, University of Leeds, UK)

3.2 Cherenkov radiation

It is not possible to directly measure HE γ-rays due to the opaqueness of the Earth's atmosphere. However, when colliding with existing particles in the atmosphere, γ-rays generate showers of particles. Most of the particles in the atmosphere have relativistic velocities. Those particles Cherenkov Telescopes (IACTs) located on the ground. Cherenkov radiation can also happen in water [6].

Cherenkov radiation (named after Soviet physicist Pavel Cherenkov) is produced when a rapid

[1] https://www.iap.kit.edu/corsika/

particle travels through a medium at a constant velocity v higher than the speed of light in that material [10]. If n denotes the medium's refractive index then the threshold velocity equals $\beta = \frac{1}{n}$ [3]. Emission angle for Cherenkov radiation is:

$$\theta_c = arccos\frac{1}{n\beta} \tag{3.1}$$

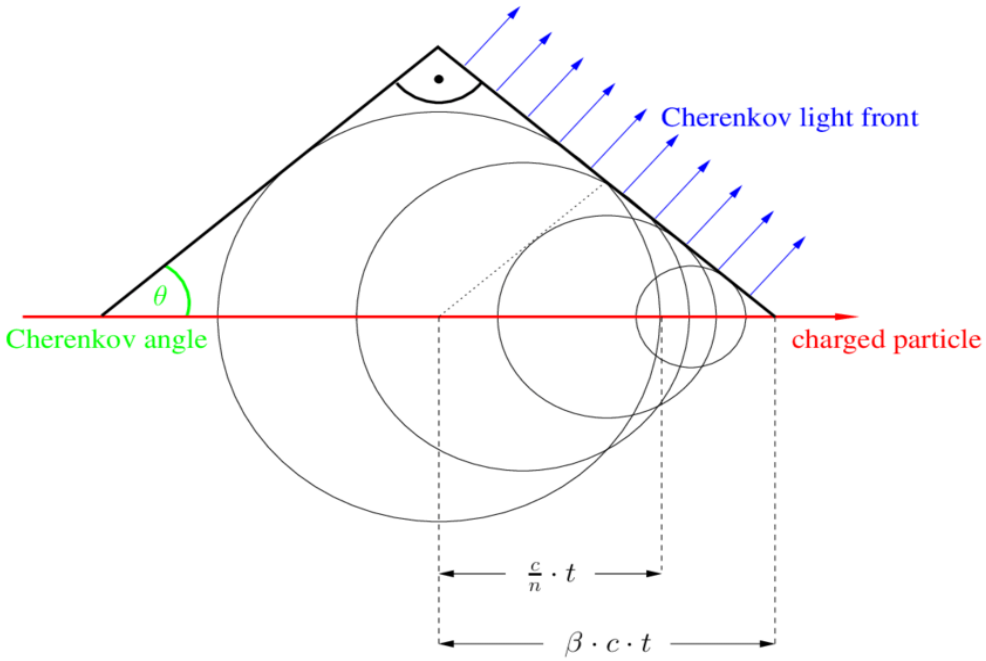

Figure 6: Interpretation of the Cherenkov effect. (Image taken from [15])

Since Cherenkov radiation depends on the wavelength detectors are sensitive to near UV region $(300 - 350nm)$ [6].

3.3 EBL

VHE photons coming from various astrophysical sources can be absorbed on extragalactic background photons of lower energies. The process is called pair creation ($\gamma_E + \gamma_\epsilon \rightarrow e^+ + e^-$) and the wavelenghts of the photons go from the cosmic microwave background (CMB) to near-ultraviolet.

The extragalactic background light (EBL) is the name for background radiation in ultraviolet, optical and near-infrared [6]. The light was emitted by diverse sources, i.e. AGN, stars, galaxies, through the entire cosmic history. Modifications of the light were made due to the existing redshift.

Having that said it can be assumed that EBL contains significant information of universes' structure and evolution [6].

It is possible to determine the density of EBL photons. Those values are shown in the Figure 7.

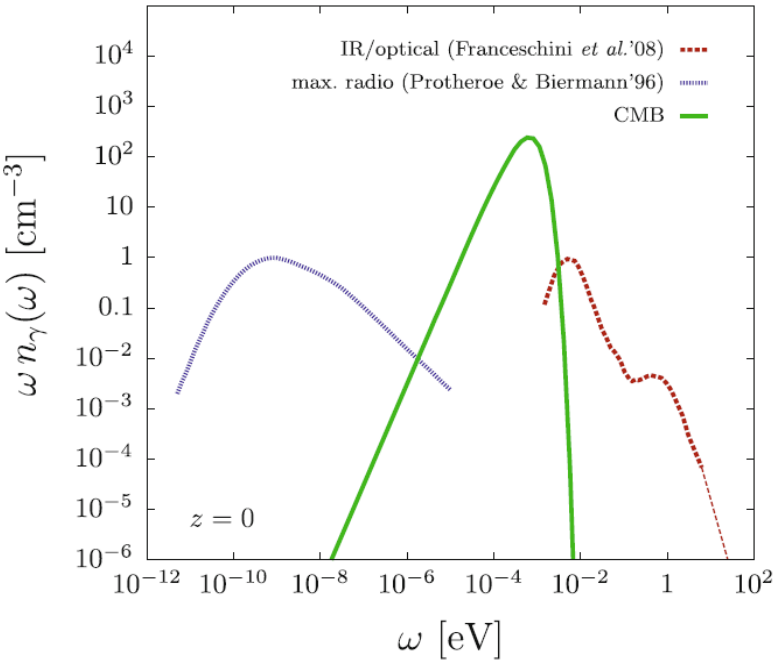

Figure 7: Estimation of photon number density made up of the radio background, the CMB and EBL (IR/optical/UV). (Image taken from: [16])

As it can be seen from the figure, the majority of the EBL is found in the $\sim 10^{-3} - 10eV$ energy range, which corresponds to wavelengths from infrared to the near-ultraviolet [6]. The UV to IR part of EBL mostly comes from direct starlight and AGN, while the closer it gets to the milimetre part of the spectrum it is made from dust particles that have been re-emited [6]. Since nearby objects and galactic light can contaminate direct measurements of the EBL, plenty of uncertainties occur.

3.4 MAGIC telescopes characteristics

MAGIC telescopes is a system of two 17 m diameter IACT. They detect showers of particles that originated from galactic or extragalactic γ-rays. Stereoscopic mode is used to enable simultaneous operation of the telescopes. The the full three-dimensional reconstruction of air showers is possible because the identical event is observed by two telescopes at slightly different angles.

Figure 8: The MAGIC telescopes. (Credit: Daniel Lopez (IAC))

Due to their light structure, repositioning time is rapid enough to catch short phenomena like GRBs. That is possible due to a steel construction constructed of six bogeys and a circular rail that allow motion in two perpendicular axis, a vertical axis for azimuth adjustments and horizontal axis that is in control of telescope elevation.

The mirror dish of the telescopes is composed by 246 mirrors of size 99x99 cm. Each telescope has an active reflective mirror surface of 236 m^2. Mirrors are made by aluminium or glass: they reflect in the camera the Cherenkov light produced by relativistic charged particles in the atmosphere. They are mounted on three different points (one is fixed, two are movable). Each mirror has a max deviation of $< 10\mu m$ from an ideal paraboloid and the average reflectivity, (measured on a spot of 2 cm radius at wavelengths between 290-650 nm), is around 80%.

On each telescope a $1m$ diameter camera is installed and the camera has 1039 photomultiplier tubes (PMTs) that represent individual pixels and a field of view (FoV) of $3.5°$. PMTs output are electrical pulses that are then transformed in optical signals. Ultra fast PMTs as well as read out electronics are of great importance so that the time component can be used in the shower reconstructions.

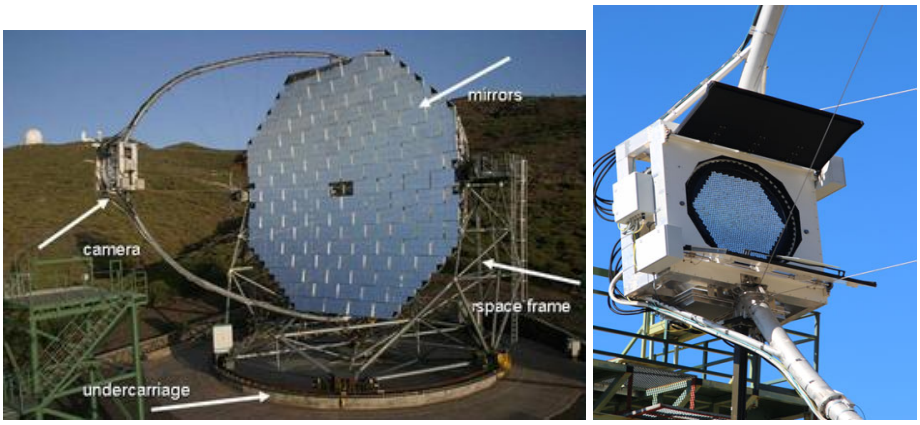

(a) Structure of the telescope. (Image taken from the MAGIC Telescopes webpage [2])

(b) Enlarged photo of the camera with PMTs. (Image taken from the MAGIC Telescopes webpage [3])

Figure 9: Picture of MAGIC telescope.

In order to get the background estimations at the same time while observing the source there is an offset from the camera center by $0.4°$. That is called wobble mode (shown in Figure 10), and the offset is inverted every 20 minutes in order to have fewer uncertainties.

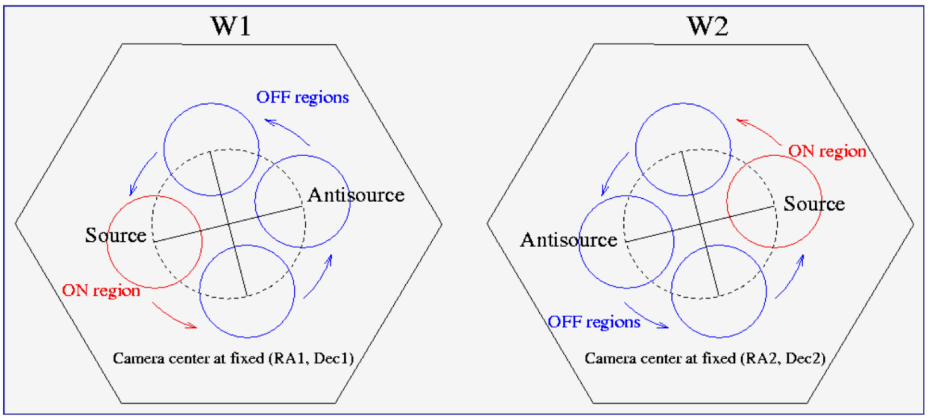

Figure 10: Wobble observations with two different pointings W1 and W2, and a possible choice of OFF regions. From the MAGIC Data Analysis manual.

When MAGIC started operations, it was composed by only one telescope, MAGIC I. In 2009 MAGIC II was installed and since then MAGIC is operating mainly in stereo mode. The stereo

[3]https://magic.mpp.mpg.de/newcomers/technical-implementation/mirrors/
[3]https://magic.mpp.mpg.de/newcomers/technical-implementation/camera/

configuration has improved sensibly the performance and the sensitivity of MAGIC, as can be seen from Fig. 11. Improvements on the sensitivity come also from the upgrade of the readout of the telescopes and the upgrade of the camera of MAGIC I in 2012. The current sensitivity is indicated by the red points.

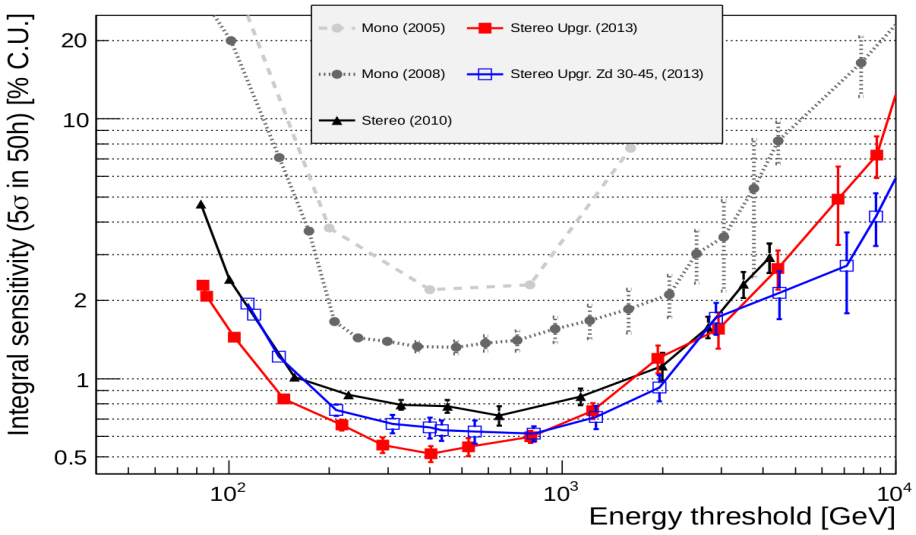

Figure 11: Evolution of integral sensitivity of the MAGIC telescopes. (Image taken from: [17])

3.5 High energy γ-rays

The energy range from 100MeV to 100GeV is the so called high-energy (HE) γ-ray range. HE and VHE γ-rays studies are strongly interconnected. In the broadband Spectral energy distribution (SED) of astrophysical sources, when γ-ray emission is present, the HE and VHE γ-ray define a bump in the broadband SED which is often attributed to Inverse Compton (IC) process. The study of combined HE-VHE spectra is for this reason very important, and many studies are conducted combining HE with VHE spectra to investigate the IC bump of broadband SEDs. In particular, the Fermi Large Area Telescope (LAT), on board of the Fermi satellite, is overlapping with MAGIC energy range around 10-100GeV, and this is extremely useful to constrain modelings in the high energy γ-rays range.

3.5.1 Fermi-LAT

The Fermi Space Telescope has two types of detectors; Large Area Telescope (LAT) and Gamma-ray Burst Monitor (GBM).

LAT is a HE γ-ray telescope that measures energies from 20 Mev to 300 GeV. It measures energy, direction and time of arrival for γ-rays. To be able to make such measurements incident γ-ray has to make an interaction that results in an electron positron pair. For that purpose there are 16 modules that each contains a converter-tracker and a calorimeter. The converter-tracker consists of 16 planes made of tungsten which make the conversion to e^-e^+ possible. It is possible to track the path of those particles due to silicon-slip detector, and use that information to recreate the direction of incident γ-rays. The calorimeter has two main purposes: measurement of energy deposition that occurred during the EM shower in tungsten foils, to provide a shower development profile. There is also Anticoincidence detector (ACD) that rejects charged particles with high efficiency. The Monte Carlo simulations of the events have a significant role in the creation of the reconstruction.

Objective of GBM is to obtain data that will enable Fermi observatory to be reoriented in order to get a reading of GRB while in the LAT's field of view (FoV). That kind of response is possible with MC simulations. GBM can also be triggered by solar flares and terrestrial flashes, but focus can also be put on background data that can be useful for further analysis and numerous other studies. Another goal of GBM is to make an analysis of spectra along with LAT. Since there are two types of detectors on GBM where one measures low-energy spectrum from 8 keV, and the other goes up to 40 MeV, together with LAT data a cross-calibration can be provided.

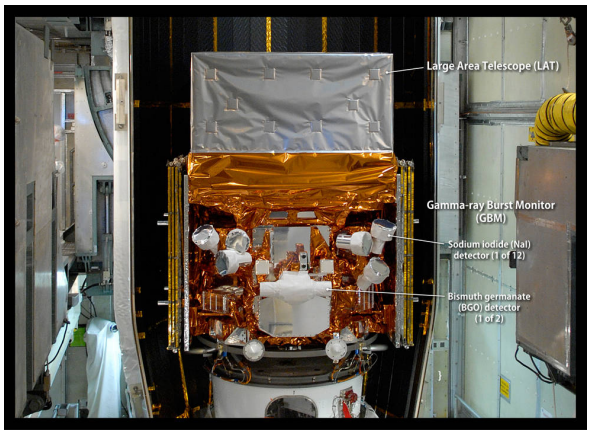

(a) Photo of Fermi Gamma-ray Space Telescope with marked detectors of GBM. (Credits: NASA/Jim Grossmann)

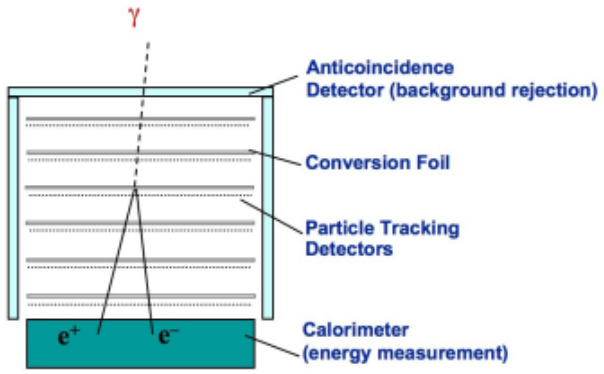

(b) Illustration of LAT. (Image taken from Fermi LAT collaboration site)

Figure 12: Detectors of Fermi Space Telescope
[4]

[4]https://www-glast.stanford.edu/instrument.html

3.6 New generation of IACTs

3.6.1 Cherenkov Telescope Array (CTA)

Cherenkov Telescope Array (CTA) will aim to unify photon observatories with neutrino and gravitational wave ones. It will try to: improve sensitivity of current instruments, enable access to whole sky, improve detection area and provide a larger energy coverage. Extensive energy range will be provided so that the whole low energy universe as well as extreme accelerators (highest energies) can be observed in detail. FoV will be increased due to the numerous telescopes [18].

CTA will include two array sites (La Palma and Chile) as well as three offices, two in Germany and one in Italy. The headquarters will be placed in Bologna [5].

4 DATA ANALYSIS

For the analysis MARS (MAGIC analysis and reconstruction software) package is used. Each telescope is treated separately at first, and the conversion to photoelectrons (phe) is done. Next is time image cleaning where the viable pixels are chosen by searching boundary and core ones. Afterwards the images from two separate analysis are combined to get needed 3D parameters. Random forest (RF) method is used to separate showers of hadron origin from the electromagnetic ones, and by averaging the individual energy estimators from the two telescopes, the energy of an event is calculated. By reconstructing the direction of an observed particle without the timing information angular resolution and sensitivity are worse than when the timing information is included.

There are also several systematic uncertainties: atmospheric conditions that change during the observations, lacking knowledge in reflectivity of the mirrors with dust deposit that varies with every observation, amount of the night sky background (NSB) that is higher during moonlight and twilight observations and varies with each source, mispointing of one or both telescopes, dissimilarities of data and reconstructed spectra with MC simulations.

[5] https://www.cta-observatory.org/about/array-locations/

4.1 MAGIC analysis chain

Standard stereo analysis chain in MAGIC consists of several steps. In low-level data processing an extensive amount of data is being processed. Firstly a conversion to root format is needed (Merpp). Secondly, calibrations of charge and time have to be done (Sorcerer), and lastly the images have to be cleaned and parametrization has to be made (Star). The process is usually done by OSA (on site analysis), and can be redone in PIC (Port d'Informació Cientifica) server if needed.

The intermediate stage is done by analysers. Images from both telescopes, and from same event, have to be merged (SuperStar). Training of the energy estimation, γ/hadron separation and position reconstruction (Coach) is required so it can be applied to the MC's and the data (Melibea).

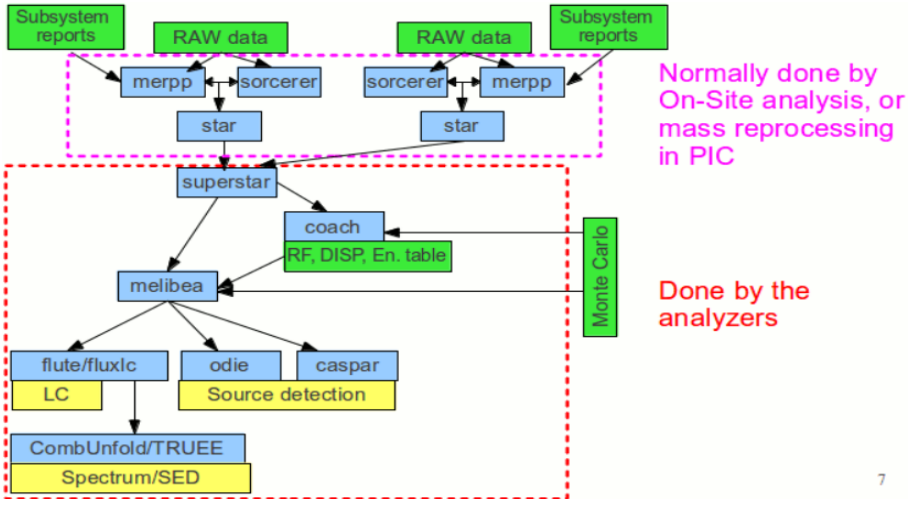

Figure 13: MAGIC analysis chain. (Credit: Julian Sitarek, from MAGIC Data Analysis Manual)

4.2 High level of data analysis

High level data analysis provides the SED's, skymaps, lightcurves using several MARS programs.

4.2.1 θ^2 plots

Using Melibea files, with program Odie, θ^2 plots are made. θ^2 plots are squared angular distance among the true source location in the camera and reconstructed source position. It is separately done for three different energy ranges: low energies ($\sim$100GeV), full range ($>$ 250GeV), high energies ($>$ 1TeV). Significance is also automatically calculated following [19]. This analysis results in several On and Off plots which are used to prove the detection of a source in case of a significance $> 5\ \sigma$. In γ-ray astronomy is very important to assess background fluctuations in order to measure the accuracy

of the discovery of sources. This is why the Gaussian standard deviation σ is used to describe the probability of an excess of events caused by a legitimate source. The likelihood ratio test is used to determine this probability.

4.2.2 Skymaps

Caspar, as Odie, is a program that uses Melibea files for the analysis. Its purpose is to create Skymaps. Those are two-dimensional images of the measured photons with automatically applied wobble correction and they show the RA (Right Ascension) and DEC (Declination) of the object. With that kind of visualisation it is possible to confirm if the observed AGN is point-like, as well as significance. As a final product, several outputs are made, but the one that will be mentioned in this work of thesis due to undetected sources, is TS (Test Statistics) value map. Our test statistic is the eq. 17 of [19], applied on a smoothed and modeled background estimation. Its null hypothesis distribution mostly resembles a Gaussian function. The TS value distributions are compared to a Null Hypothesis distribution, which is calculated on the fly using a Toy-MC, and the actual background map.

4.2.3 Flux calculations and Upper limits

In order to obtain flux calculations, number of γ-rays, observation time and collection area are needed. The rate of γ-rays per unit area is γ-ray flux:

$$\Phi = \frac{d^2 N_\gamma}{dSdt} \tag{4.1}$$

Energy flux per unit energy, or simply, spectral energy distribution (SED) is:

$$\frac{E^2 d\Phi}{dE}(TeVcm^{-2}s^{-1}) = \frac{Ed\Phi}{d(logE)} \tag{4.2}$$

If N_{ON} is number of events that contain both source signal and background, N_{OFF} is background number of events and α is the ratio between ON and OFF regions, then the number of γ-rays is acquired from θ^2 plots aplying equation:

$$N_{excess} = N_{ON} - \alpha * N_{OFF} \tag{4.3}$$

The time between the start and finish of the observations and the effective observation time are not the same due to gaps in taking data and dead time during which no additional incoming events may be processed by the detector. Intuitively, region of a perfect detector that would gather γ-rays at a similar

rate to the actual MAGIC detector is called effective collection area:

$$A_{eff} = \int_{-\infty}^{\infty} \epsilon(x, y) dx dy \tag{4.4}$$

For lower zenith distances (ZD) the energy threshold is lower, and for higher ZDs the energy treshold is higher and therefore effective collection area is larger. The effective area also depends on selection cuts as well as relative orientation of the telescopes.

The light curve displays the time evolution of integral flux (Φ). Φ has to be calculated above a certain energy and it can be predicted from the observations as:

$$\Phi_{E>E_0} \approx \frac{N_{excess, E_{est}>E_0}}{t_{eff} \langle A'_{eff} \rangle_{E>E_0}} \tag{4.5}$$

For $\langle A'_{eff} \rangle_{E>E_0}$ calculations a certain spectral shape has to be assumed. Also, the effective area needs to be averaged according to the zenith angle distribution in each time bin. N_{excess} statistical uncertainty propagates to flux uncertainty.

In case of a faint signal corresponding to a significance lower than 5σ (no detection), differential and integral upper limits are calculated. For calculating differential flux UL statistical procedure in [20] is followed. The method and terminology applied are those explained in [21]. Computation of confidence intervals is one of the challenges an experimental physicist will encounter when working with upper limits since limits in general are a specific case of confidence intervals and statistical precision of measurements is depicted in confidence intervals.
In MAGIC, upper limits are calculated at 95% C.L. In particular, we can obtain through the program flute, upper limits for the integral flux (lightcurve) and for the SED.

4.2.4 Unfolding

In the MAGIC standard analysis chain, the unfolding is used to obtain the "true energy" (E_{true}) distribution from distribution of "estimated energy" (E_{est}). True here refers to the fundamental gamma's actual energy, which is undetermined for real data but a starting point for MC simulations. The result given by the look-up tables during the data processing, assuming a clear sky, is the estimated energy. The method of unfolding (or deconvolution) transforms the space of observables to the space of sought parameters and takes migration effects caused by limited acceptance and resolution into account. A migration matrix describes the "passage" from E_{est} to E_{true}. Due of the several possible unfolding algorithms and their numerous parameters, unfolding is a particularly challenging numerical problem and each of the algorithms result in a different spectrum. Furthermore, unfolded data has linked er-

rors. Solutions are fluctuating when unfolding noisy data. In this work of thesis, the usual unfolding was not performed since we did not obtain spectral points: but in the program flute, a so called "poor man's unfolding" was used to obtain the upper limits. An assumption was made about the spectral shape of the observed source, which was then used to calculate the needed factors to translate the event excesses in bins of estimated energy into differential fluxes at the corresponding values of true energy.

5 RESULTS

5.1 Data sample

The results here presented regard the analysis of 5 sources observed by MAGIC telescopes but which remained un-detected. This work is part of a wider project which aims to publish all the upper limits from BL Lac objects undetected by MAGIC from 2016 to 2022. In this work, a catalog of all such undetected sources was created and it is presented in Figs.14 and 15. The classification of the source, the time of observation, the significance of the signal obtained from a fast analysis performed at that time the morning after the observation, and other information are gathered in the catalog. From the initial 41 sources identified, we selected 5: 4FGL-J0955.1+3551, 87GB-225250.5+235403, TXS1700+685, PKS2247-131 and PKS2345-16. Since the MAGIC data available for such undetected sources are stored on tape and not directly available for download, we focused on data from 2020 to 2022. The rest of the data will be analysed for the paper in preparation and compared with results obtained with another software, named gammapy[6]. The analysis conducted in the present work has been performed with Mars, the standard MAGIC data analysis software, available to full members of the MAGIC collaboration. As the results reported here are not yet published, by MAGIC Collaboration rules they have to be considered strictly confidential.

[6]https://gammapy.org/

Name of the source	Type of source	Time of observation	detection	significance of the signal
3C 345	fsrq	7/4/2022 and 24/4/2022		-2.0 sigma (FR)
Ton116	bl lac	5/3/2022 and 6/3/2022		-1.2 sigma (LE)
SDSSJ1430+2303	seyfert	3-7/3/2022		-2.3 sigma (LE)
TXS1902+556	bl lac	20/7/2021		0.96 sigma (FE)
TXS1700+685	seyfert	17/3/2021, 16-19/5/2021, 30-31/5/2021, 1/6/2021, 11-12/6/2021	Fermi LAT	2.3 sigma (LE)
4C55.17	fsrq	10/12/2019 and 4/5/2021		-1.2 sigma (LE)
OP313	fsrq	21-23/6/2019, 25-31/12/2019, 20/2/2021, 18/4/2021	Fermi LAT	-1.78 sigma (2019)
87GB 225250.5+235403	bl lac	18/11/2020		1.07 sigma (FR)
PKS 2247-131	bl lac	7-9/11/2020	Fermi LAT	1.54 sigma (FR)
PKS2345-16	fsrq	24/10/2020	Fermi LAT	1.67 sigma (LE)
OV591	fsrq	8-9/10/2020	Fermi LAT	1.57 sigma (LE)
TXS 0025+197	fsrq	2-4/9/2019, 29-30/11/2019, 1/12/2019, 18-21/8/2020	Fermi LAT	-2.69 sigma (FR)
RBS1752	bl lac	13/8/2020		-1.18 sigma (HE)
4FGL J0955.1+3551	bl lac	17-18/1/2020		-1.66 sigma (HE)
TXS 0358+210	fsrq	18/12/2019	Fermi LAT	-1.71 sigma (LE)
RBS 42	extreme	6/2019 - 12/2019		0.8 sigma (max 2.0)
3FGLJ0115.8+2519	bl lac	25-26/7/2017 and 27/11/2019		1.65 sigma (LE)
GB6J0540+5823	bl lac	5/11/2019		2.04 sigma (LE)
4C +39.12	radiogal	9/2019 - 11/2019		-0.80 sigma (LE)
PKS1502+106	bl lac	1-2/8/2019	Fermi LAT	-1.40 sigma (LE)
B2 2234+28A	bl lac	3 and 12/7/2019		1.26 sigma (FR)
CGRaBSJ0211+1051	bl lac	1-4/7/2019	Fermi LAT	2.08 sigma (LE)
2FHL J2209.8-0451	bl lac	29 and 30/5/2019		0.66 sigma (LE)
FermiJ1544-0	bl lac	09/04/2019	Fermi LAT	2.66 sigma (LE)
GB6-J0540+5823	bl lac	4/3/2019		-0.88 sigma (LE)
S4 1800+44	fsrq	7/3/2019	Fermi LAT	-0.87 sigma (LE)
B2 0234+285	fsrq	31/01/2019, 01/02/2019 and 1/3/2019		1.45 sigma (FR)
PKS0346-27	fsrq	27/01/2019	Fermi LAT	-1.40 sigma (FR)
TXS 2010+463	bl lac	27/11/2018		-1.01 sigma (LE)
BZB J0022+0006	extreme	24-25/07/2018, 3/08/2018, 2-4/09/2018, 03/10/2018		-1.18 sigma (FR)
RGB J1756+553	extreme	1/07/2018, 3/07/2018, 5-7/07/2018, 18-23/07/2018		-1.94 sigma (LE) or 2.01 (HE)
3C 371	bl lac	9/2016 and 4/2018		1.67 ('16); -0.01 ('18)
1RXS J055717.0-061705	extreme	2018	Fermi-LAT	-1.4 sigma
TXS0149+710	bl lac	30/8/2017 and 14/9/2017		-2.24 sigma (LE)
TXS 2241+406	fsrq	31/7/2016, 1/8/2016, 29/08/2017, 02/09/2017 (3 pages)	yes	2.79 sigma (LE)
PKS 0507+17	fsrq	15-16/3/2017	Fermi LAT	1.26 sigma (FR)
OJ 287	bl lac	12/02/2016, 13/02/2016, 16/02/2017, 17/02/2017		2.39 sigma (3.31 with 5off)
BZBJ1417+2543	extreme	2017		-1.1 sigma (FR)
CTA 102	fsrq	11/2016 and 12/2016	Fermi-LAT	2.37 sigma
3FGLJ2346+0705	bl lac	8/2016 and 10/2016		1.18 sigma
AO 0235	bl lac	30/12/2015 - 12/1/2016	Fermi LAT	1.64 sigma (FR)

Figure 14: Catalog of undetected AGNs by MAGIC. In this table, type of sources, observation time and significance of the signal from the fast analysis are reported.

Name of the source	redshift	Effective time(dark/moon)		weather conditions	LIDAR trans	zenith
		dark	moon			
3C 345	0.595	0.9 h	/	/	0.7	19-36 and 32-45
Ton116	1.066	1.2 h	/		0.95	18-27 and 19-31
SDSSJ1430+2303	0.081	4.5 h	/		0.85	5-32
TXS1902+556	0.58	1.0 h	/	/	/	36-42
TXS1700+685	0.301	8.8 h	/		0.5-0.8	39-51
4C55.17	0.902	1.48 h	/		0.75	26-35
OP313	0.997	7.8 h	/		0.75	5-35
87GB 225250.5+235403	/	/	0.8 h		/	4-9
PKS 2247-131	0.22	3.78 h	/		/	41-50
PKS2345-16	0.576	/	0.98		/	45-48
OV591	1.22	2.7 h	/		/	22-36
TXS 0025+197	1.55	11.43 h	/		/	5-37
RBS1752	0.45	0.7h	<--		/	37-38
4FGL J0955.1+3551	0.557	/	/		/	/
TXS 0358+210	0.83	0.67 h	/		/	11-16 deg
RBS 42	0.1	13.8 hours	6.6 hours	3 nights not good	0.8	0 to 50 deg
3FGLJ0115.8+2519	0.375	2.56 h	/		0.8	4-14 and 17-35
GB6J0540+5823	/	0.97 h	/		/	29-31 deg
4C +39.12	0.028	13.1 hours	/	CloudinessMax: 45	0.7	< 50 degree
PKS1502+106	1.838	/	/		/	29-48 deg
B2 2234+28A	0.795	2.3 h	/		0.8	0 - 36 deg
CGRaBSJ0211+1051	0.2	1.9 h	/		0.8	50 - 65 deg
2FHL J2209.8-0451	0.396	1.62 h	<--		/	/
FermiJ1544-0	/	1 h	/		/	52-60
GB6-J0540+5823	/	0.5 hrs	/	Maximum cloudiness=45	/	35-40
S4 1800+44	0.663	0.8 hrs	/	Maximum cloudiness=45	0.8	30-40
B2 0234+285	1.21	2.26h + 0.8 h	/	Maximum cloudiness=45	0.9	12.0 - 30.9 and 40 - 60
PKS0346-27	0.991	1h	<--		0.82	56.1 - 57.4
TXS 2010+463	/	0.96 h	<--	/	0.8	36-48 deg
BZB J0022+0006	0.31	15 total	<--	cloudiness at 45.	0.85	/
RGB J1756+553	0.065	/	~21.6 h		0.55	~25-50°
3C 371	0.051	5.6 h + 3.4h	/	cloudinessMax: 45	0.55('16), 0.85('18)	34-50('18)
1RXS J055717.0-061705	0.2	18 h	5.4 h		0.55	5-50 deg
TXS0149+710	0.022	0.97 + 0.64	<--		0.7	5 - 50
TXS 2241+406	1.17	5.79 h	<--	/	0.7	20-60 and 5-50
PKS 0507+17	0.416	1.09 h	<--		?	5-50
OJ 287	0.306	6.1 hours	<--	cloudinessMax: 45	0.55 and 0.85 ('17)	5-50
BZBJ1417+2543	0.243	1.1 h	/	/	0.55	30-50 deg
CTA 102	1.032	8.4 h	<--		0.55-0.85	5-50
3FGLJ2346+0705	0.17	14.7h	<--	Cloudiness < 45	0.7	< 35°
AO 0235	0.94	4.89h	<--		/	/

Figure 15: Catalog of undetected AGNs by MAGIC. In this table, redshifts, effective time, weather conditions, LIDAR transmission values and zenith angle of the observations are reported.

5.2 4FGL J0955.1+3551

4FGL J0955.1+3551 is a BL Lac source located at a redshift of z=0.557. It was observed by MAGIC on 17.1.2020. and 18.1.2020. in the zenith range 15-50. The coordinates of the source are: RA[h] 9.918855, DEC[deg] 35.850250

This source is located within the 90% localization region of a neutrino event detected from IceCube, 200107A., and X-ray activity was detected by Swift-XRT telescope [22, 23].

The source was observed in dark conditions, and the quality cuts were performed using the LIDAR transmission. Events with transmission below 0.7 were discarded. The amount of effective time after cuts, as indicated in Fig. 16, was 2.81 h. The significance of the signal was negative in both FR and LE range of the θ^2 plots. To obtain the θ^2 plots, only one simultaneous background region was considered (1 OFF setting).

5.2.1 θ^2 Plots

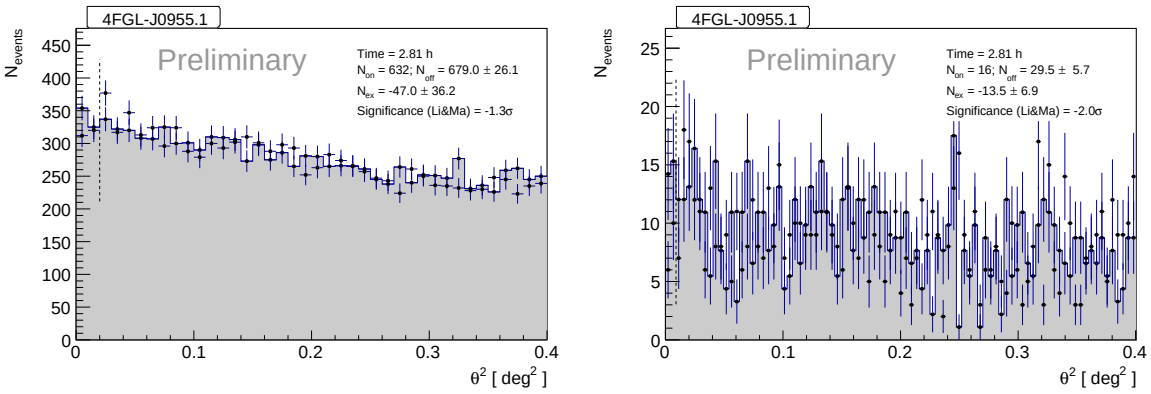

(a) LE range cuts

(b) FR range cuts

Figure 16: θ^2 plots for 4FGL J0955.1+3551

5.2.2 Skymaps

The skymaps were obtained with the program caspar, and as in odie the 1 OFF setting was used for the bakground estimation.

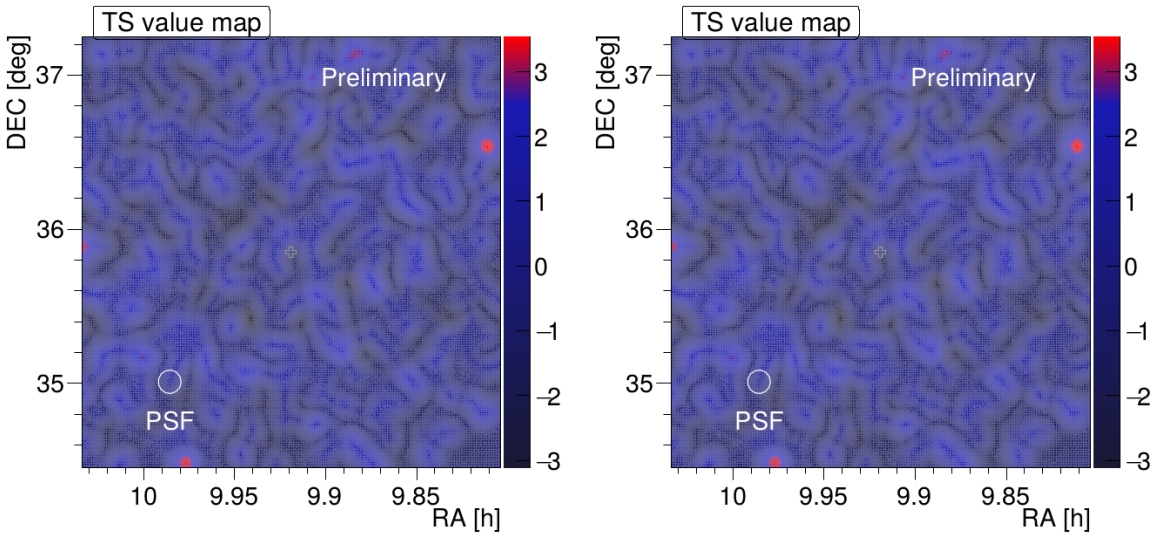

(a) LE range cuts

(b) FR range cuts

Figure 17: Skymaps for 4FGL J0955.1+3551

5.2.3 Flux calculations and upper limits

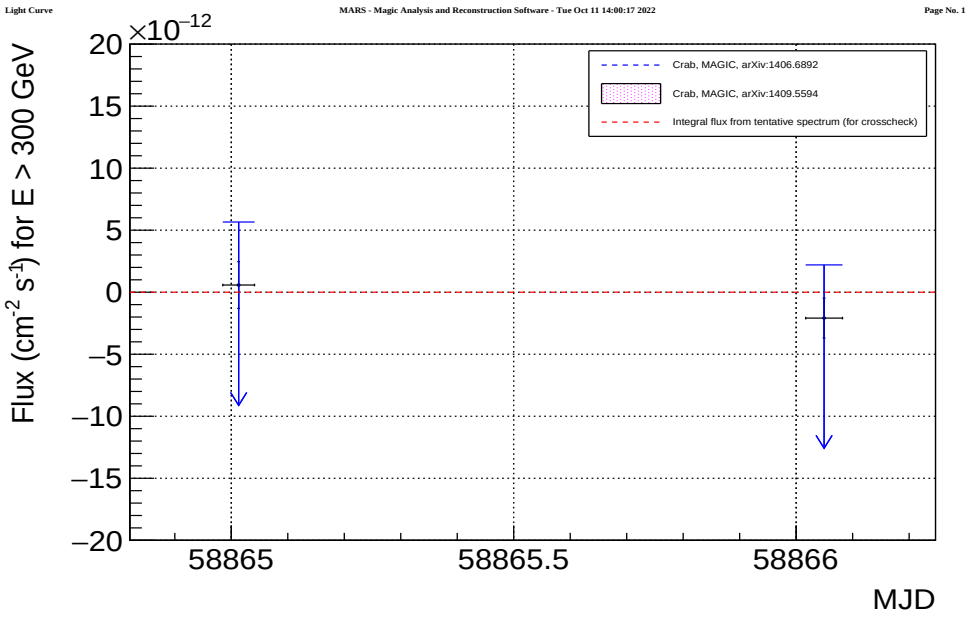

Figure 18: LC

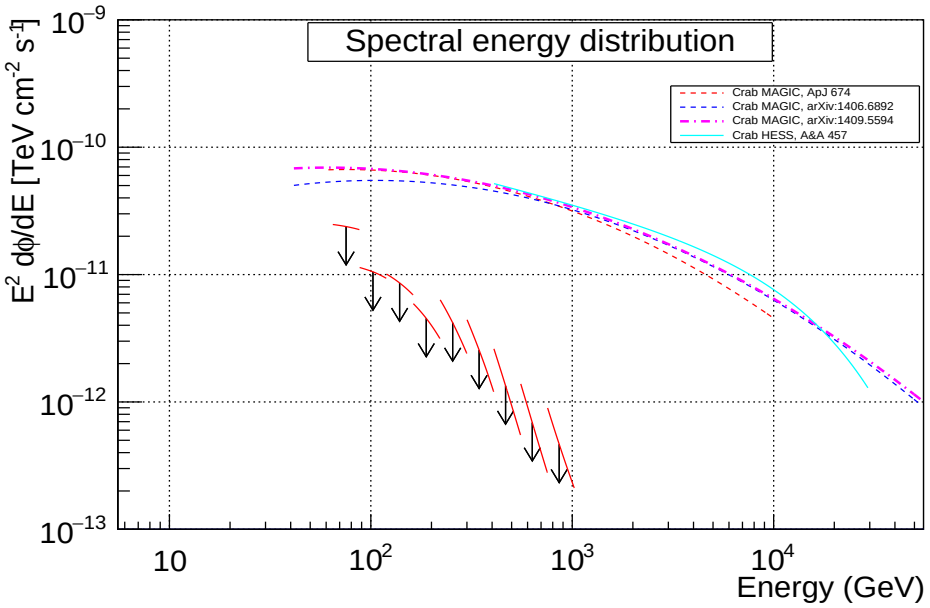

Figure 19: SED

5.3 87GB-225250.5+235403

87GB-225250.5+235403 is a BL Lac source with a redshift of z=1.359. It was observed by MAGIC on 18.11.2020. in the zenith range 0-35. The coordinates of the source are: RA[h] 22.920833, DEC[deg] 24.169722

The source was observed in low moon conditions, and the quality cuts were performed using the LIDAR transmission. Events with transmission below 0.7 were discarded. The amount of effective time after cuts, as indicated in Fig. 20, was 3.99 h. The significance of the signal was positive in FR range and negative in LE range of the θ^2 plots. To obtain the θ^2 plots, only one simultaneous background region was considered (1 OFF setting).

5.3.1 θ^2 Plots

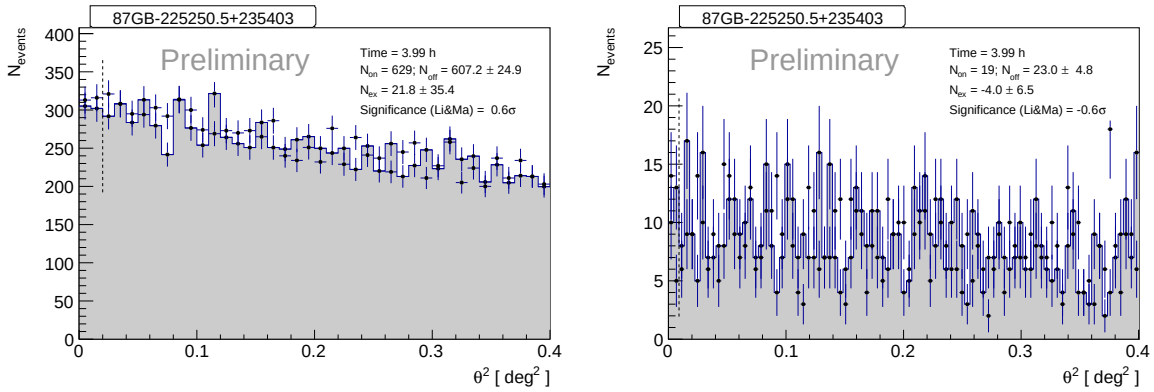

(a) LE range cuts (b) FR range cuts

Figure 20: θ^2 plots for 87GB-225250.5+235403

5.3.2 Skymaps

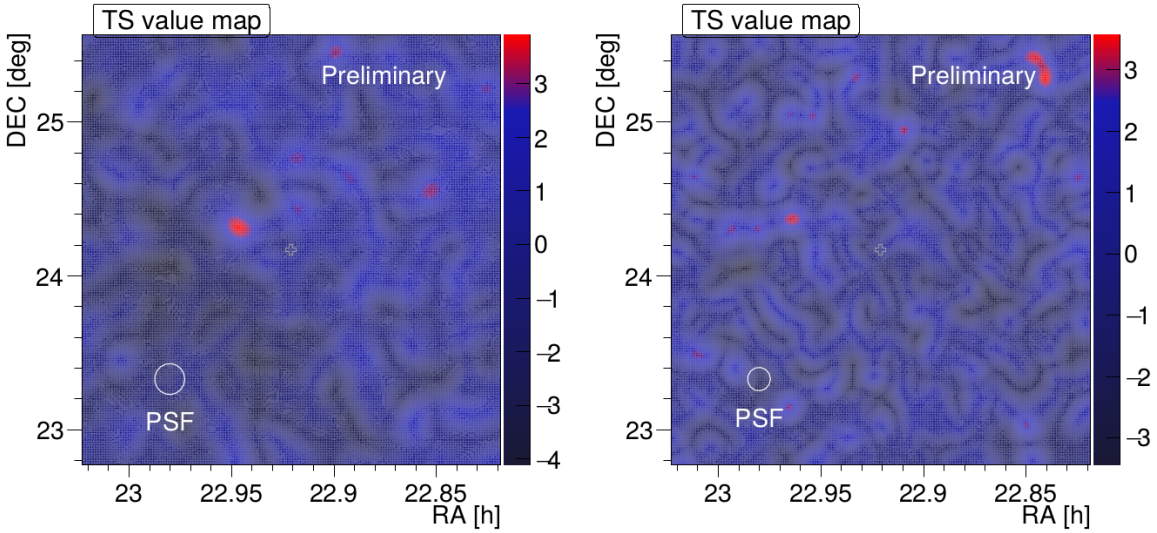

(a) LE range cuts (b) FR range cuts

Figure 21: Skymaps for 87GB-225250.5+235403

5.3.3 Flux calculations and upper limits

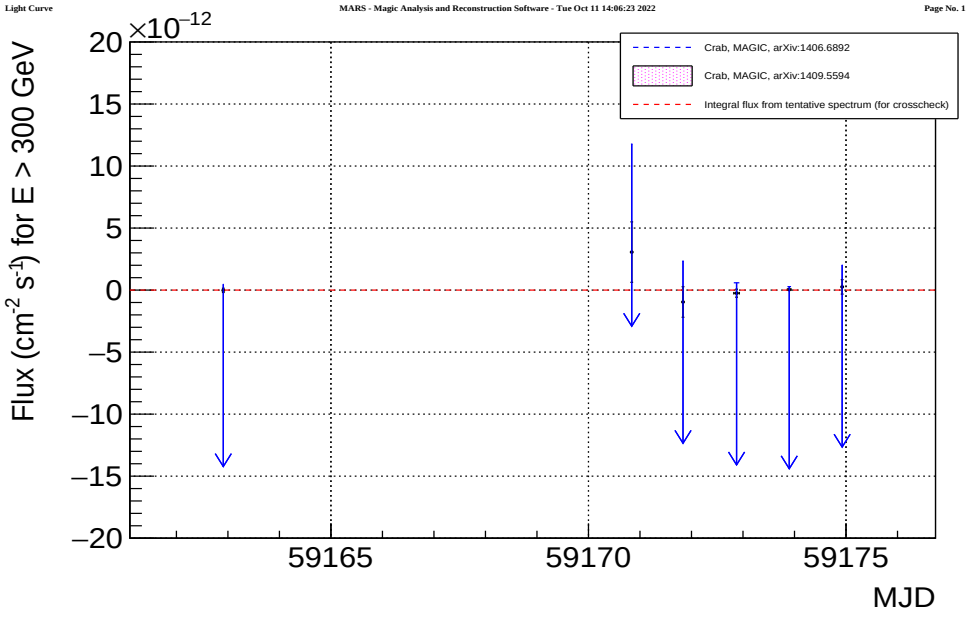

Figure 22: LC

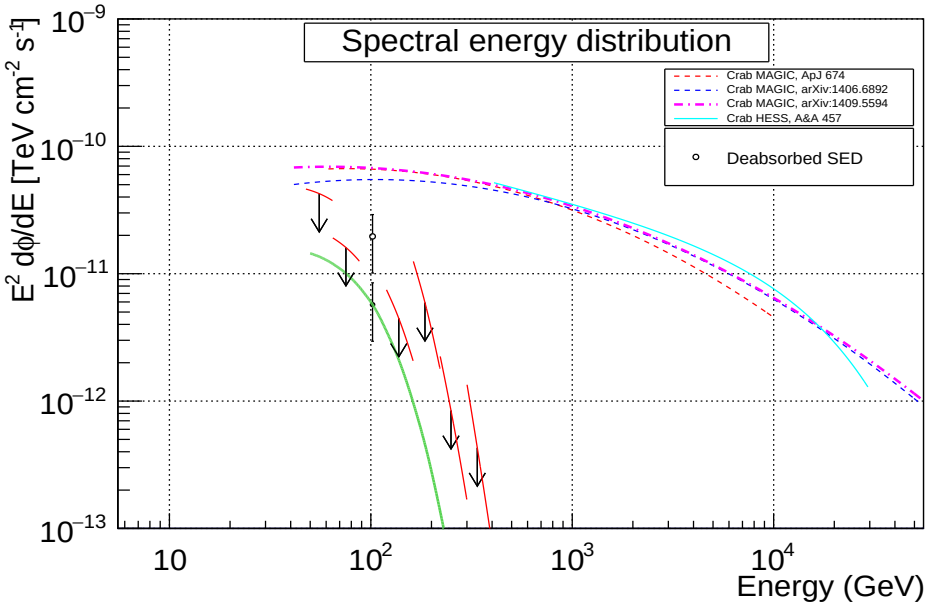

Figure 23: SED

5.4 TXS17000+685

TXS17000+685 is a radio galaxy located at a redshift of z=0.301. It was observed by MAGIC on: 17.3.2021., 16-19.5.2021., 30 and 31.5.2021., 1.6.202., 11 and 12.6.2021. in the zenith range 0-65. The coordinates of the source are: RA[h] 17.002580, DEC[deg] 68.501913

The source was observed in dark conditions, and the quality cuts were performed using the LIDAR transmission. Events with transmission below 0.7 were discarded. The amount of effective time after cuts, as indicated in Fig. 24, was 5.77 h. The significance of the signal was positive and below 1σ in both FR and LE range of the θ^2 plots. To obtain the θ^2 plots, only one simultaneous background region was considered (1 OFF setting).

This source has been detected by Fermi-LAT and there it is classified as FSRQ [24]. According to preliminary research the source had heightened γ-ray emission on 15.3.2021. [24]

5.4.1 θ^2 Plots

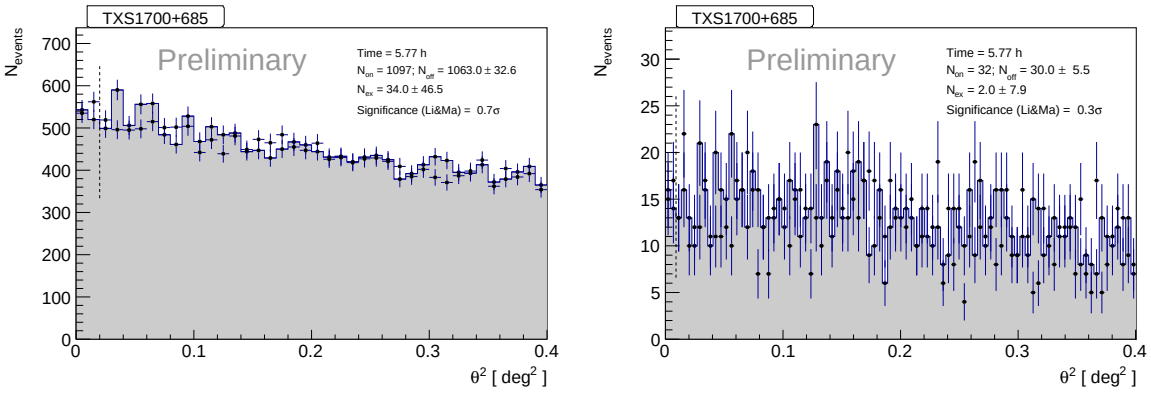

(a) LE range cuts

(b) FR range cuts

Figure 24: θ^2 plots for TXS17000+685

5.4.2 Skymaps

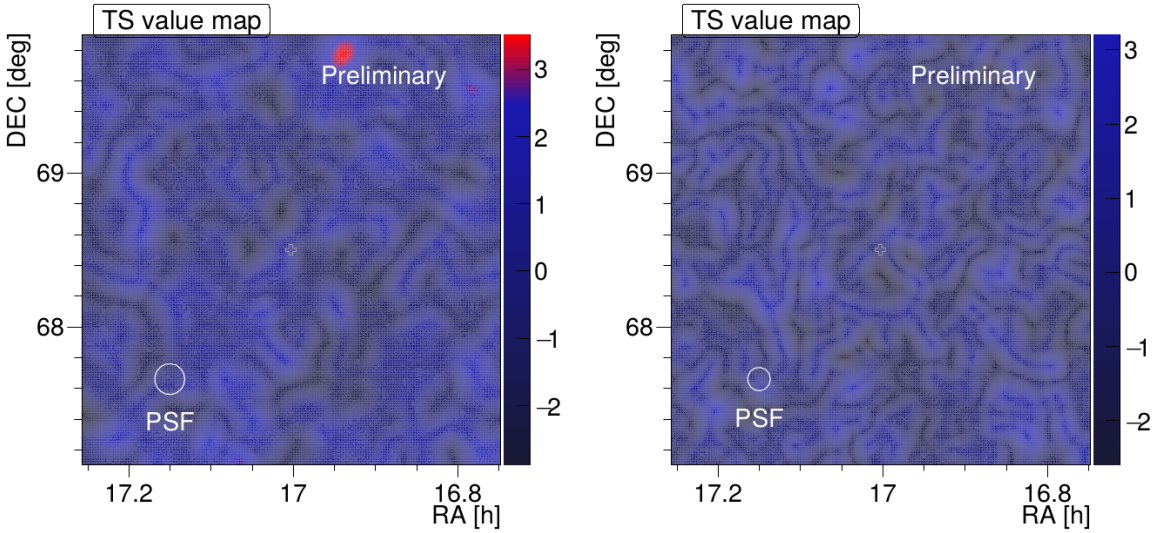

(a) LE range cuts

(b) FR range cuts

Figure 25: Skymaps for TXS17000+685

5.4.3 Flux calculations and upper limits

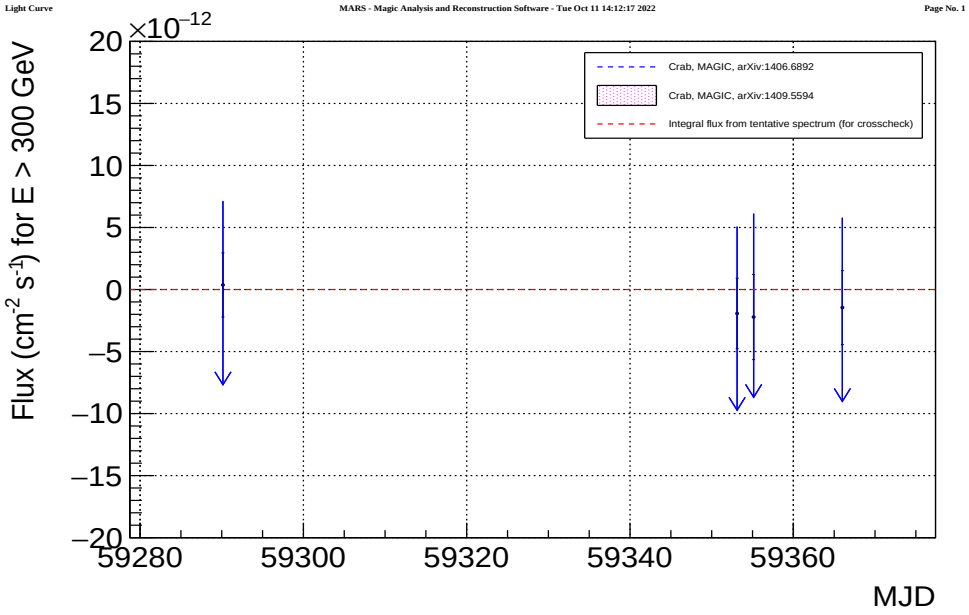

Figure 26: LC

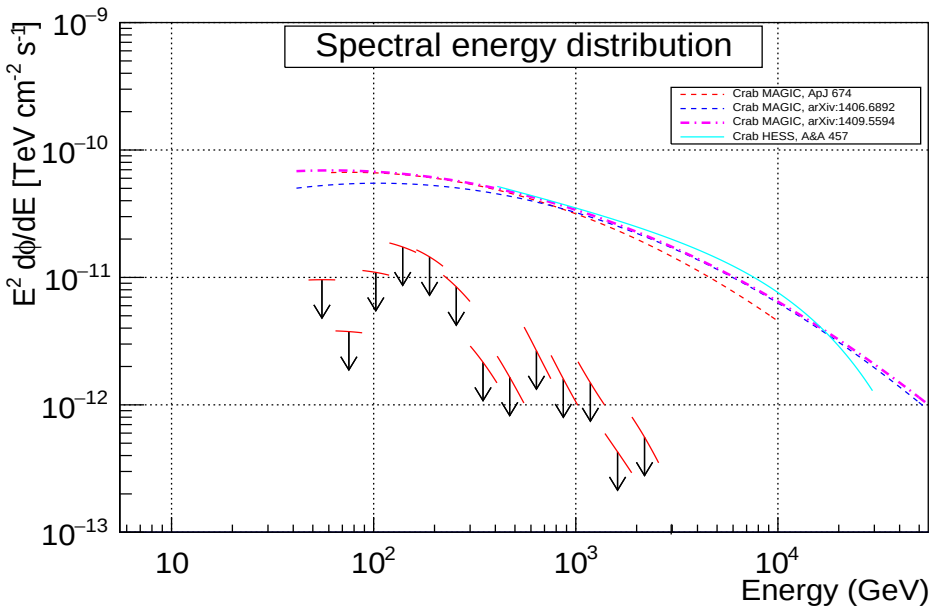

Figure 27: SED

5.5 PKS2247-131

PKS2247-131 is a BL Lac source located at a redshift z=0.22. It was observed by MAGIC on 7.11.2020., 8.11.2020. and 9.11.2020. in the zenith range 40-55. The coordinates of the source are: RA[h] 22.833333, DEC[deg] -12.854722

The source was observed in dark conditions, and the quality cuts were performed using the LIDAR transmission. Events with transmission below 0.7 were discarded. The amount of effective time after cuts, as indicated in Fig. 28, was 3.79 h. The significance of the signal was positive in FR and negative in LE range of the θ^2 plots. To obtain the θ^2 plots, only one simultaneous background region was considered (1 OFF setting).

This source has been detected by Fermi-LAT [25]. Weak absorption lines were observed in the optical spectrum, and a quasi periodic oscillation of 34.5 days was reported.

5.5.1 θ^2 Plots

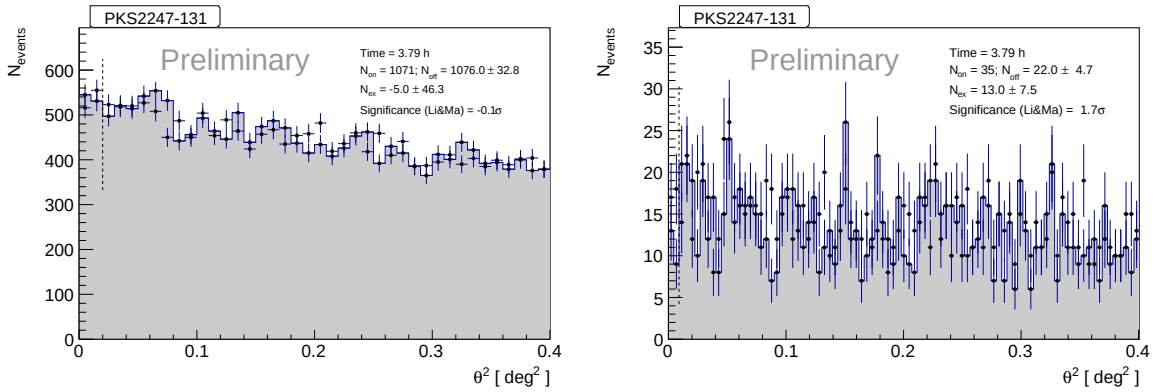

(a) LE range cuts

(b) FR range cuts

Figure 28: θ^2 plots for PKS2247-131

5.5.2 Skymaps

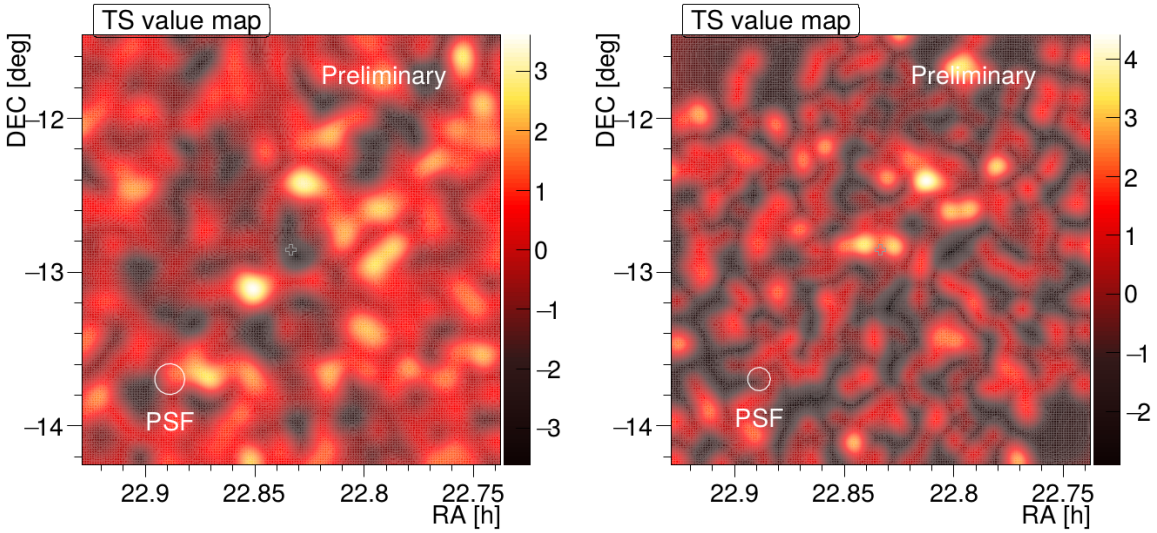

(a) LE range cuts

(b) FR range cuts

Figure 29: Skymaps for PKS2247-131

5.5.3 Flux calculations and upper limits

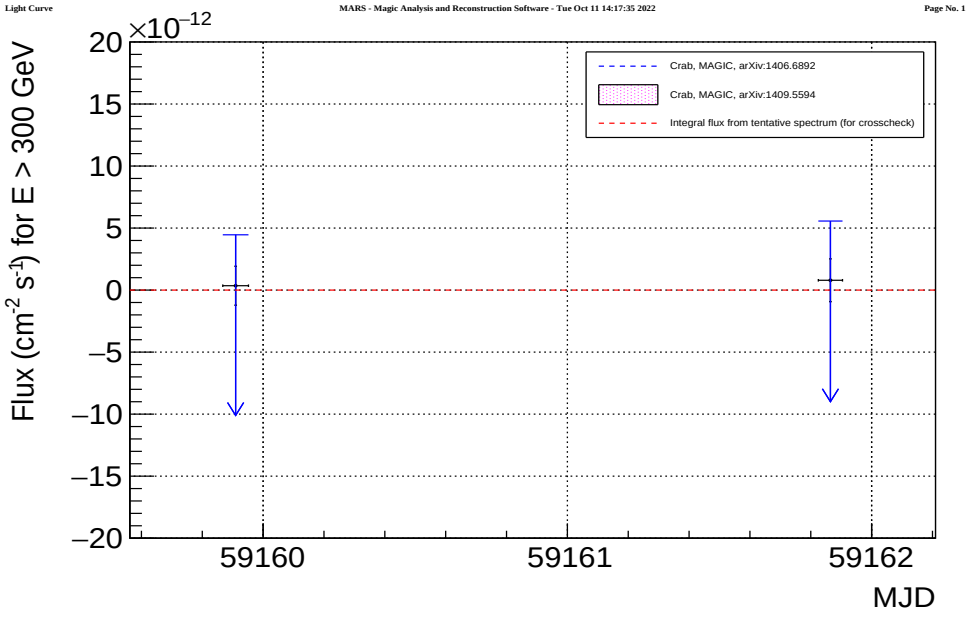

Figure 30: LC

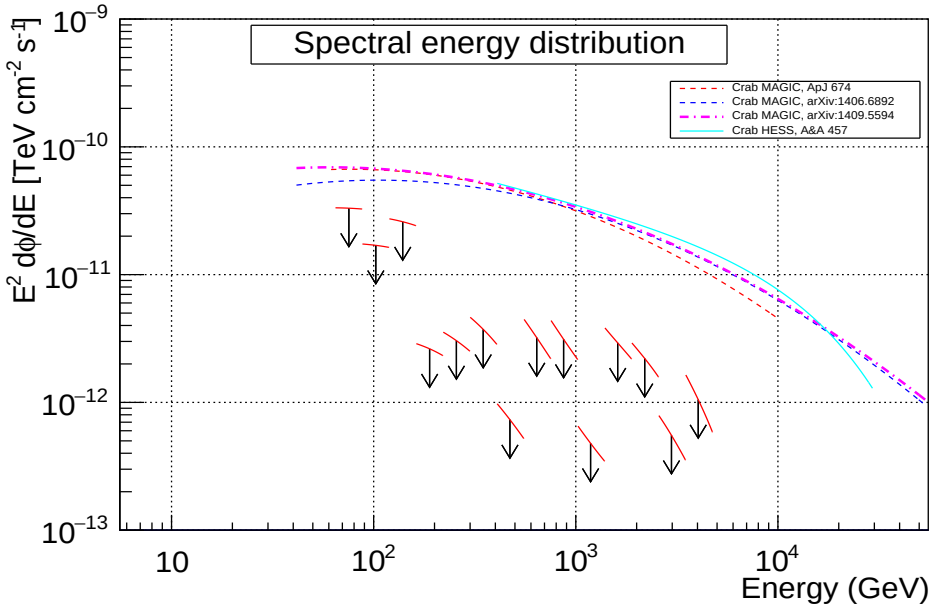

Figure 31: SED

5.6 PKS2345-16

PKS2345-16 is a FSRQ located at a redshift z=0.576. It was observed by MAGIC on 24.10.2020. in the zenith range 40-50. The coordinates of the source are: RA[h] 23.800278, DEC[deg] -16.519722

The source was observed in moon conditions, and the quality cuts were performed using the LIDAR transmission. Events with transmission below 0.7 were discarded. The amount of effective time after cuts, as indicated in Fig. 32, was 0.98 h. The significance of the signal was positive in FR and negative in LE range of the θ^2 plots. To obtain the θ^2 plots, only one simultaneous background region was considered (1 OFF setting).

This source has been detected by Fermi-LAT [26]. According to preliminary research the source had heightened γ-ray emission on 5.10.2019. [26]

5.6.1 θ^2 Plots

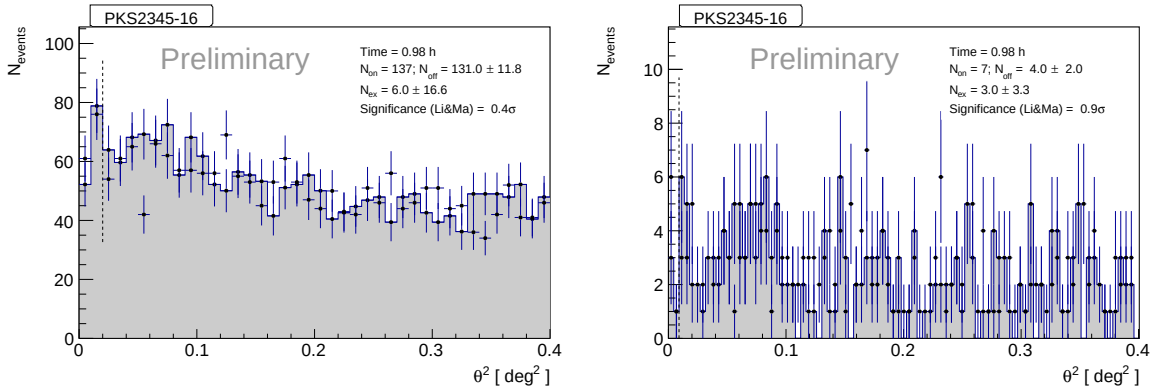

(a) LE range cuts

(b) FR range cuts

Figure 32: θ^2 plots for PKS2345-16

5.6.2 Skymaps

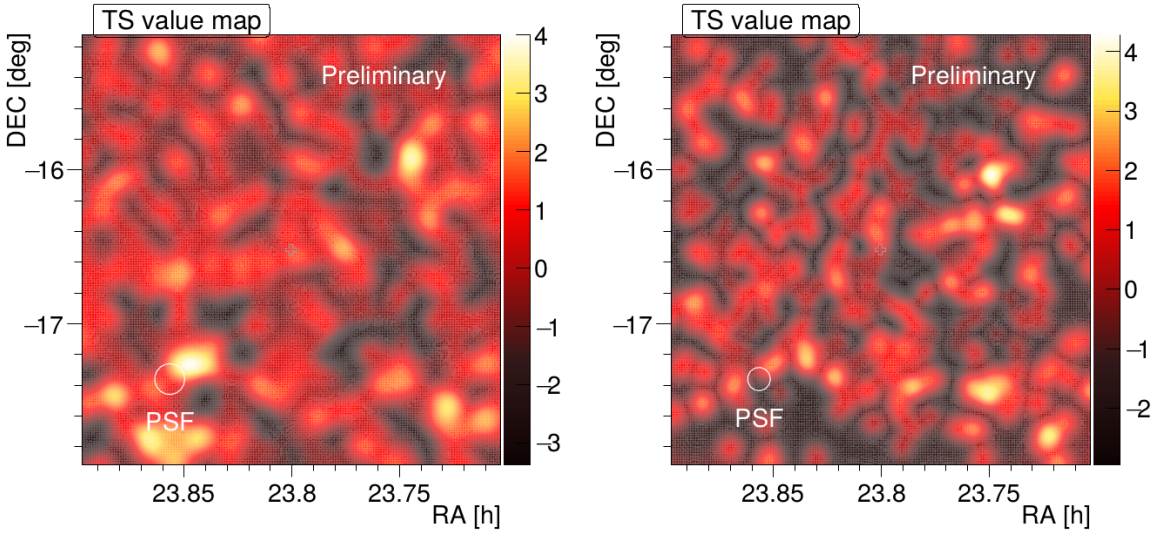

(a) LE range cuts

(b) FR range cuts

Figure 33: Skymaps for PKS2345-16

5.6.3 Flux calculations and upper limits

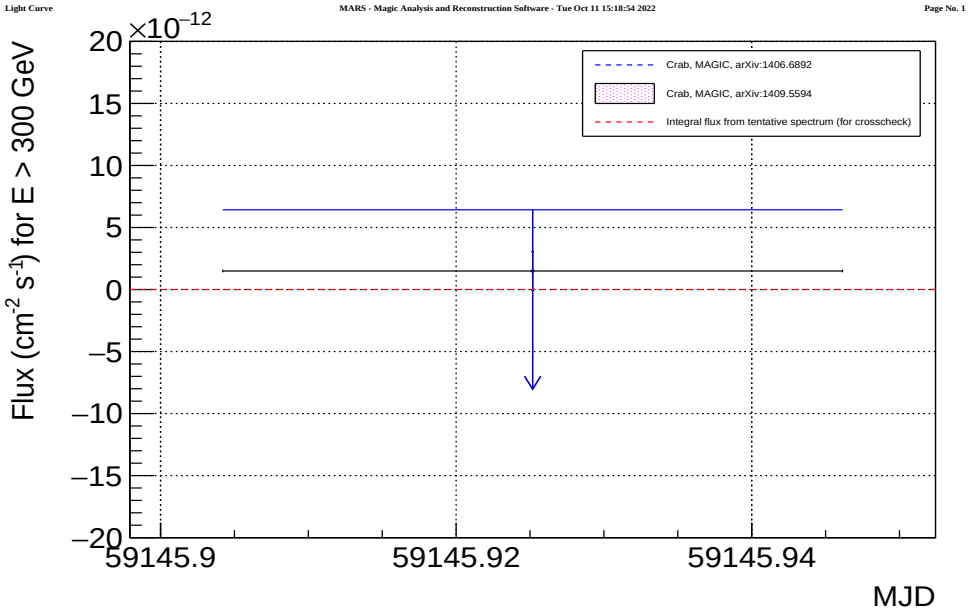

Figure 34: LC

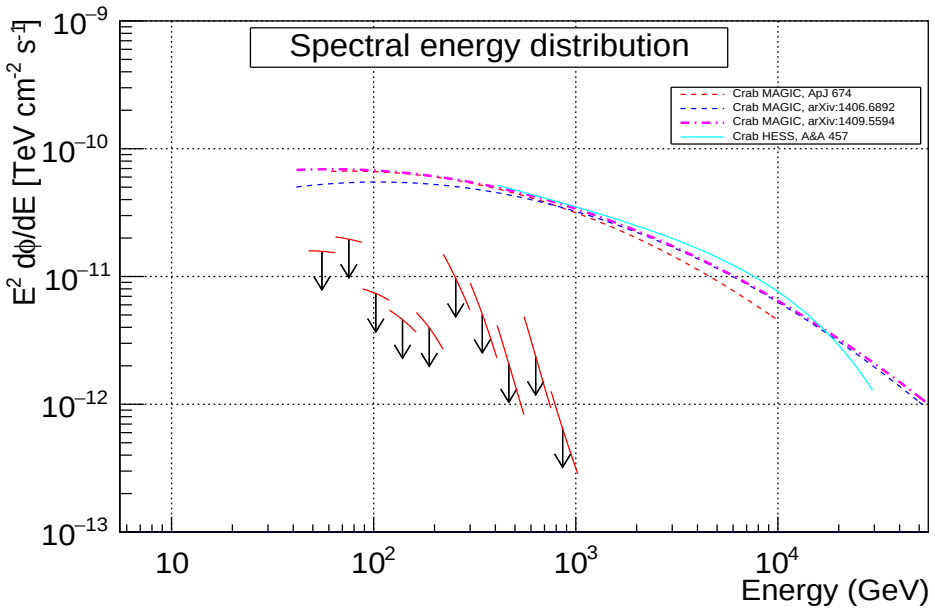

Figure 35: SED

5.7 TXS1902+556

TXS1902+556 is a BL Lac source located at a redshift z=0.58. It was observed by MAGIC on 20.7.2021. in dark conditions. Due to bad weather conditions, no events have survived the quality cuts.

5.8 Comparison with fast analyses

The sources object of this study were observed by MAGIC within the MoToO program, an observational proposal that aims to quickly followup with MAGIC high state of sources in other wavebands and search for a detection also in VHE γ rays. Usually when one of those alerts is issued, MAGIC observes the interesting source and a fast analysis is performed as soon as the data is available, the morning after the observation. In some cases I could compare my analysis with such fast analysis and I found it to be compatible in most cases. It has to be noted, though, that the fast analysis is rarely conducted in case of non-detection, so the available fast analyses are not always including the full data sample used in this work, but few nights of observations. Following, the upper limits reported by the fast analysis (left) and the ones obtained for the present work (right). The fast analysis can not be used for publication, so the paper in preparation will not include such analysis. The reason is that the fast analysis aims to just quickly evaluate if the source is detected, often without even calculate upper

limits. On the other hand, we show here the comparison as a quick confirmation of non-detection.

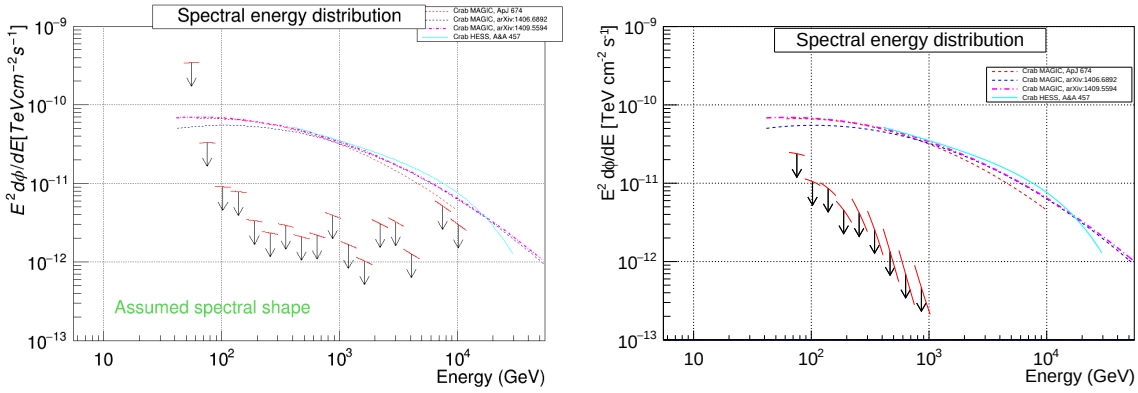

(a) Fast analysis (b) Present work

Figure 36: 4FGL-J0955.1+3551

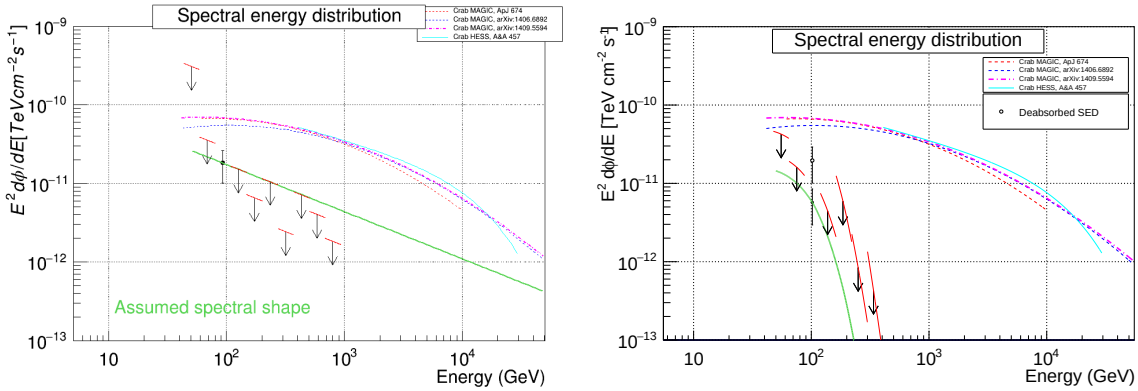

(a) Fast analysis (b) Present work

Figure 37: 87GB-225250.5+235403

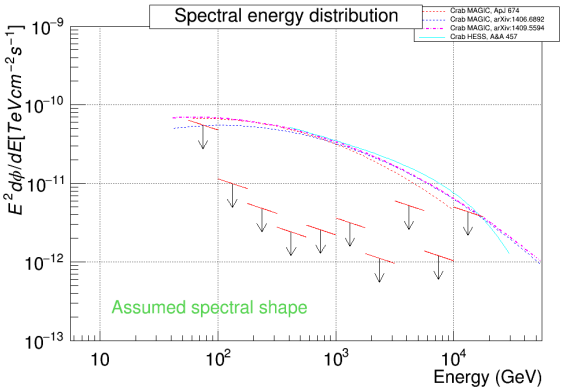

(a) Fast analysis

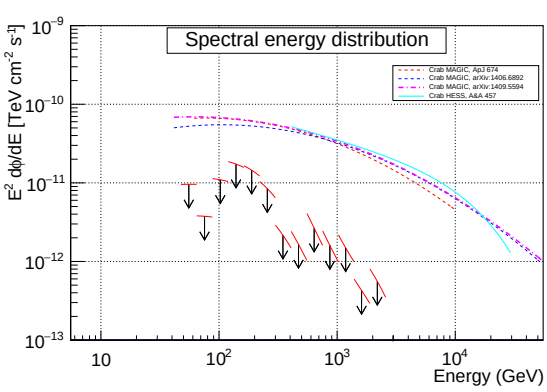

(b) Present work

Figure 38: TXS1700+685

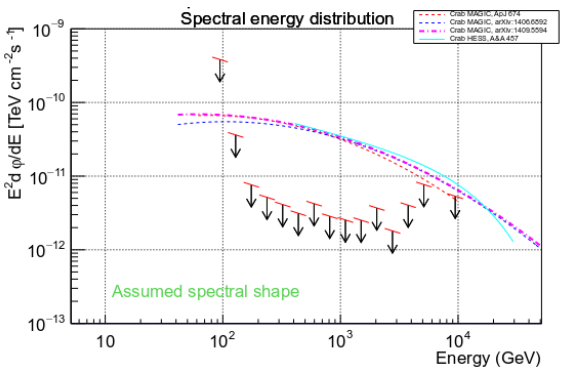

(a) Fast analysis

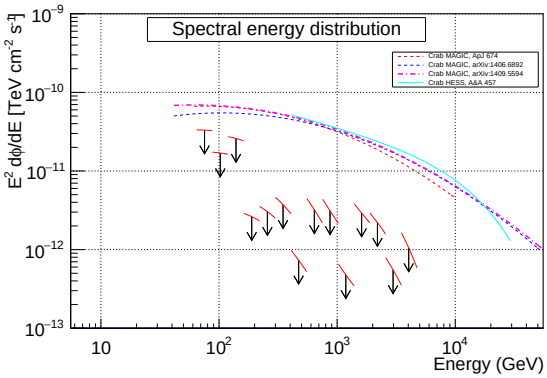

(b) Present work

Figure 39: PKS2247-131

6 CONCLUSIONS

In this work of thesis, a catalog of sources observed by the MAGIC telescopes but not detected has been created. From a list of 43 sources, 25 BL Lac objects were identified and a sample of 5 sources has been selected as starting point for a long-term upper limits study with MAGIC data.
The 5 sources analysed for this work of thesis are: 4FGL-J0955.1+3551, 87GB-225250.5+235403, TXS1700+685, PKS2247-131 and PKS2345-16.
Using the Mars (MAGIC reconstruction software) data analysis suite, θ^2 plots, skymaps, upper limits on the lightcurves and on the SEDs of all the 5 sources were produced. The results will be used in a work in preparation for MAGIC on upper limits of BL Lac sources.

References

[1] IceCube Collaboration et al. Multimessenger observations of a flaring blazar coincident with high-energy neutrino IceCube-170922A. *Science*, 361(6398):eaat1378, July 2018. doi: 10.1126/science.aat1378.

[2] Abbott, B.P. et al. Observation of Gravitational Waves from a Binary Black Hole Merger. , 116 (6):061102, February 2016. doi: 10.1103/PhysRevLett.116.061102.

[3] De Angelis, A. and Pimenta, M. *Introduction to Particle and Astroparticle Physics*. 2018. doi: 10.1007/978-3-319-78181-5.

[4] Czerny, B. and Naddaf, M.H. Accretion in Active Galactic Nuclei. In *Accretion Processes in Cosmic Sources - II*, page 6, September 2018.

[5] Peterson, B.M. *An Introduction to Active Galactic Nuclei*. 1997.

[6] Spurio, M. *Particles and Astrophysics*. 2015. doi: 10.1007/978-3-319-08051-2.

[7] Laor, A. On the Nature of Low-Luminosity Narrow-Line Active Galactic Nuclei. , 590(1): 86–94, June 2003. doi: 10.1086/375008.

[8] Elitzur, M. and Shlosman, I. The AGN-obscuring Torus: The End of the "Doughnut" Paradigm? , 648(2):L101–L104, September 2006. doi: 10.1086/508158.

[9] Zier, C. and Biermann, P.L. Binary black holes and tori in AGN. II. Can stellar winds constitute a dusty torus? , 396:91–108, December 2002. doi: 10.1051/0004-6361:20021339.

[10] Longair, M.S. *High Energy Astrophysics*. 2011.

[11] Khachikian, E.Y. and Weedman, D.W. An atlas of Seyfert galaxies. , 192:581–589, September 1974. doi: 10.1086/153093.

[12] Dermer, C.D. and Giebels, B. Active galactic nuclei at gamma-ray energies. *Comptes Rendus Physique*, 17(6):594–616, June 2016. doi: 10.1016/j.crhy.2016.04.004.

[13] Fanaroff, B.L. and Riley, J.M. The morphology of extragalactic radio sources of high and low luminosity. , 167:31P–36P, May 1974. doi: 10.1093/mnras/167.1.31P.

[14] Hillas, A.M. Cerenkov Light Images of EAS Produced by Primary Gamma Rays and by Nuclei. In *19th International Cosmic Ray Conference (ICRC19), Volume 3*, volume 3 of *International Cosmic Ray Conference*, page 445, August 1985.

[15] Gluesenkamp, T. *On the Detection of Subrelativistic Magnetic Monopoles with the IceCube Neutrino Observatory*. PhD thesis, 01 2010.

[16] Ahlers, M. et al. GZK neutrinos after the Fermi-LAT diffuse photon flux measurement. *Astroparticle Physics*, 34(2):106–115, September 2010. doi: 10.1016/j.astropartphys.2010.06.003.

[17] Aleksić, J. et al. The major upgrade of the MAGIC telescopes, Part II: A performance study using observations of the Crab Nebula. *Astroparticle Physics*, 72:76–94, January 2016. doi: 10.1016/j.astropartphys.2015.02.005.

[18] Cherenkov Telescope Array Consortium et al. *Science with the Cherenkov Telescope Array*. 2019. doi: 10.1142/10986.

[19] Li, T.P. and Ma, Y.Q. Analysis methods for results in gamma-ray astronomy. , 272:317–324, September 1983. doi: 10.1086/161295.

[20] Rolke, W.A., López, A.M. and Conrad, J. Limits and confidence intervals in the presence of nuisance parameters. *Nuclear Instruments and Methods in Physics Research A*, 551(2-3):493–503, October 2005. doi: 10.1016/j.nima.2005.05.068.

[21] Aleksić, J. et al. Searches for dark matter annihilation signatures in the Segue 1 satellite galaxy with the MAGIC-I telescope. , 2011(6):035, June 2011. doi: 10.1088/1475-7516/2011/06/035.

[22] Krauss, F. et al. Swift follow-up observations of IceCube-200107A: Identification of a X-ray high state for 4FGL J0955.1+3551. *The Astronomer's Telegram*, 13395:1, January 2020.

[23] Giommi, P., Glauch, T. and Resconi, E. Swift observation of a flaring very extreme blazar in the error region of the high-energy neutrino Ice-Cube 200107A. *The Astronomer's Telegram*, 13394: 1, January 2020.

[24] Cheung, C.C. and Angioni, R. Fermi-LAT detection of a new gamma-ray flare associated with the quasar TXS 1700+685. *The Astronomer's Telegram*, 14463:1, March 2021.

[25] Zhou, J. et al. A 34.5 day quasi-periodic oscillation in γ-ray emission from the blazar PKS 2247-131. *Nature Communications*, 9:4599, November 2018. doi: 10.1038/s41467-018-07103-2.

[26] Gasparrini, D. and Angioni, R. Fermi-LAT detection of a GeV flare from the FSRQ PKS 2345-16. *The Astronomer's Telegram*, 13172:1, October 2019.

List of Figures